Journal of Rock Mechanics and Geotechnical Engineering 11 (2019) 1119–1137

Contents lists available at ScienceDirect

Journal of Rock Mechanics and Geotechnical Engineering

journal homepage: www.rockgeotech.org

Full Length Article

Investigation of mechanical behaviour of a quasi-brittle material using Karagozian and Case concrete (KCC) model

Aria Mardalizad [a], Marco Caruso [b], Andrea Manes [a,*], Marco Giglio [a]

[a] Politecnico di Milano, Department of Mechanical Engineering, Milan, Italy
[b] Politecnico di Milano, Material Testing Laboratory, Milan, Italy

ARTICLE INFO

Article history:
Received 13 September 2018
Received in revised form
18 December 2018
Accepted 9 January 2019
Available online 19 June 2019

Keywords:
Finite element method (FEM)
Triaxial compression test
Brazilian disc test
Quasi-brittle behaviour
Karagozian and Case concrete (KCC) model

ABSTRACT

The mechanical behaviour of a quasi-brittle material, i.e. Pietra Serena sandstone, was investigated both numerically and experimentally in order to build a reliable numerical modelling system applicable to more complex cases. The Karagozian and Case concrete (KCC) model was exploited as the material constitutive law and a new method to utilise this model for efficient and accurate simulation of quasi-brittle materials is discussed. The capability of this model is evaluated by comparing the results of the numerical simulations with the corresponding experimental results, and the method itself is critically assessed.

1. Introduction

This article aims to assess the suitability of a realistic material description in the rock mechanics domain. Understanding mechanical behaviour of quasi-brittle material is crucial in many scientific and industrial sectors, such as deep well drilling (Pepper, 1954; Hu and Randolph, 1998), and underground mining (Lacy and Lacy, 1992; Brady and Brown, 2013). Although the knowledge of the mechanical behaviour of quasi-brittle material has been advanced by the developments of numerical analyses and computer resources, the analysis of quasi-brittle materials' failure modes is still a crucial issue (Santarelli and Brown, 1989; Chen and Egger, 1999), with added complexity due to the sensitivity to confining stress, associativity flow, strength and post-failure deformations, localisation, etc. (Martin, 1993; Malvar and Crawford, 1998; Li et al., 2003; Jaeger et al., 2007; Brady and Brown, 2013). For this, the mechanical properties of a quasi-brittle material were investigated in this study to promote the understanding and the future design demands of this domain.

The term 'quasi-brittle' is used for materials including rock (Labuz et al., 1985), concrete (Cornelissen et al., 1986) and most ceramics. Quasi-brittle materials exhibit both moderate strain hardening (before reaching their ultimate strength) comparable with metallic materials and sharp softening responses reminiscent of brittle material (Huang and Karihaloo, 1993), and their nonlinear response has been analysed by several constitutive equations (Bai et al., 1999; Jing and Hudson, 2002). The common frameworks implemented in the finite element method (FEM) for geological constitutive modelling are based on the theoretical concepts of continuum mechanics, i.e. elasticity, plasticity (Huang and Karihaloo, 1993), damage (Rots and De Borst, 1987), visco-plasticity (Winnicki et al., 2001) and different combinations of these (Malvar et al., 2000a; Fossum and Brannon, 2004; Brannon and Leelavanichkul, 2009; Saksala, 2010).

The complex features of the quasi-brittle materials have been recently investigated and several numerical methods have been proposed (Kochavi et al., 2008a,b; Jaime, 2011; Wu and Crawford, 2015; Zhao et al., 2016). A meso-mechanical model proposed by Gary and Bailly (1998) was used to investigate the strain-rate effects on the failure behaviour of concrete under quasi-static and dynamic loadings, based on the description of the mechanisms observed at a microscopic level after failure started. The main damaging process considered in this study was the brittle tensile response induced by the Poisson's effects under compression loading. An anisotropic continuum damage model based on the micro-plane concept was proposed by Kuhl et al. (2000). Scalar damage laws of this model were formulated on different individual

* Corresponding author.
E-mail address: andrea.manes@polimi.it (A. Manes).
Peer review under responsibility of Institute of Rock and Soil Mechanics, Chinese Academy of Sciences.

https://doi.org/10.1016/j.jrmge.2019.01.005

micro-planes representing the planes of potential failure. A three-dimensional (3D) damage model with induced damage anisotropy was proposed by Desmorat et al. (2007), in which plain reinforced concrete as well as pre-stressed concrete structures was simulated by implementation of the damage model in commercially available finite element codes to high damage level inducing yielding of the reinforcement steel. The finite element code LS-DYNA was implemented in conjunction with an advanced material model, i.e. the Karagozian and Case concrete (KCC) model. The third release of the model in LS-DYNA, named *MAT_CONCRETE_-DAMAGE_REL3, was developed by Malvar et al. (1994, 1995, 1997, 2000a). This material model consists of three fixed and independent strength surfaces and decouples the deviatoric and volumetric responses. An equation-of-state (EOS) is used in conjunction with KCC material model for decoupling the volumetric and deviatoric responses. The KCC material model itself fulfils all the other input fields by an internal algorithm based on the parameter uniaxial compressive strength (UCS). However, this adjustment was originally performed based on the experimental test results of concrete, and the KCC model employing this automatic generation mode cannot realistically predict the mechanical response of quasi-brittle materials other than concrete.

This article thus aims at developing a mixed experimental-numerical approach for the calibration of the KCC material model for another type of quasi-brittle material, Pietra Serena sandstone, and at assessing its transferability in finite element analysis. For this purpose, two experimental tests, i.e. a triaxial compression test and a Brazilian disc test, were performed under several loading conditions based on the protocols of ASTM D7012-04 (2004).

The methods used and the results obtained during the experimental tests are reported in Section 2. Pietra Serena is medium-grained sandstone composed of quartz (40%), feldspars (20%), calcite (10%), micas and fragments of sedimentary (mainly carbonatic), volcanic and metamorphic rocks in terrigenous matrix (30%) (Clausi et al., 2016). This type of rock is mainly present in the Firenzuola basin (in the province of Florence, Tuscany, Italy). In Section 3, the required numerical modelling concept behind the KCC material model is described with emphasis placed on the exploitation of experimental data for the calibration of different input parameters, including also a modification resulting in tabular damage function of the KCC model, inspired by the studies of Wu et al. (2017). Even though the suggested tabular damage function is provided for Pietra Serena, the suggested method can be used to obtain tabular damage data for other materials. In Section 4, the ability of the fully calibrated material model to replicate experimental tests is analysed. Initially, the first two numerical simulations, related to the replication of triaxial compression test and Brazilian disc test, are exploited to verify the calibration process and followed by a subsequent numerical simulation implemented to replicate the flexural (four-point bending) test. This test presents a complex state of stress ranging from tension to compression and is a key test in the assessment of the calibrated model, particularly since the data from this experimental test were not used for the calibration of the model. The results of this numerical simulation are compared with the experimental test data on the same material, provided in Mardalizad et al. (2017). In the conclusion, the advantages of the new method of using the KCC material model for quasi-brittle materials other than concrete are discussed.

2. Experimental testing program

2.1. Triaxial compression test

This experimental program includes a series of triaxial tests conducted under increasing confining stresses. These tests were carried out with a triaxial apparatus of the Geotechnical Division of the Material Testing Laboratory, Politecnico di Milano (Cividini et al., 1992) by employing the protocols of ASTM D7012-04 (2004). This apparatus is mainly composed of a cell and a loading frame (see Fig. 1). The cell is designed to perform tests on the specimens with dimensions of 100 mm in diameter and up to 200 mm in height, and to withstand a confining stress up to 50 MPa.

The cell rests on a circular bottom plate of the loading frame which moves upwards to increase the axial load. The maximum capacity of the loading frame is 2200 kN. Both the confining stress and the load frame are driven by two independent servo-hydraulic systems, with a close loop control managed by a dedicated controller. The equipment allows the performance of either pressure/load-controlled or displacement-controlled tests or a combination of the two.

The feedback control for the confining stress includes a pressure transducer HBM - Model P3M (measuring range of 0–50 MPa, and accuracy of 0.2%), while the applied force is measured by a load cell BLH - Model CP21 (capacity of 2225 kN, and accuracy of 0.05% rated

Fig. 1. Triaxial testing apparatus used (Cividini et al., 1992).

output). The axial displacements between the upper and the lower surfaces of the specimen are measured by means of an external frame, which lies on an aluminium rod, in contact with the top surface of the specimen through a top cap hole, and which, at its bottom, holds an linear variable differential transformer (LVDT) (manufactured by LEANE, Model SE375, Class A). The LVDT, in its turn, maintains the contact with the specimen bottom base (with the help of a second aluminium rod inserted into a bottom hole) thanks to its return spring. Therefore, any changes in the specimen height cause a correspondent change in the transducer rod position.

The triaxial tests of this experimental campaign were performed on 5 cylindrical specimens, with an identical nominal diameter and a height equal to 100 mm and 200 mm, respectively. Each specimen was jacketed with a reinforced rubber membrane of 3 mm in thickness. After being placed on the cell base plate, the top cap was applied to the upper base and the membrane was tightened to both the top piston and the bottom base, by means of two worm gear hose clamps, to prevent the hydraulic oil from penetrating the rock during the test. Finally, the cell was assembled and inserted into a load frame with all hydraulic lines being properly connected.

All specimens (see Fig. 2) were subjected to a stress state assumed to be isotropic, starting from $\sigma_1 = \sigma_3 = 0$ and increasing up to the required value $\sigma_1 = \sigma_3 = \overline{\sigma}$ for each test (10 MPa, 20 MPa or 28 MPa) at an average constant rate of 0.3 MPa/s for both σ_1 and σ_3 (*AB*). In fact, to accurately control the isotropic stage and prevent any test failure, each stress increase was performed in two steps: an initial increase of σ_1 followed by a σ_3 increase at constant σ_1. The maximum difference between σ_1 and σ_3 was always maintained below 0.1 MPa. The specimens were then sheared under displacement control settings at a constant rate of 0.001 mm/s up to failure (*BC*).

The test results are displayed in Figs. 3 and 4 for the isotropic stress and the shear stages, respectively. Fig. 3a shows the isotropic stress state increase procedure as previously described. Fig. 3b presents the specimen deformations during this increment, showing the almost similar behaviour of all specimens except for specimen B2 which differed slightly. A similar difference is also visible in Fig. 4, in which all the shear stages of all the performed tests are compared. The maximum deviatoric stress of specimen B2 differs from the other test results, since the maximum load rises to a value comparable with the 28 MPa tests (see Table 1). Also, the initial stiffness appeared to be comparable with the 28 MPa tests. The reason of this undesired response of specimen B2 (lower compressibility in the isotropic stage and a higher resistance in the shear stage) is probably due to both the specimen arrangement in the load cell and the mechanical locking along the failure surface, which also caused an immediate decrease of deviatoric stress after failure. A comparison of the failure mode of each specimen is presented in Fig. 5.

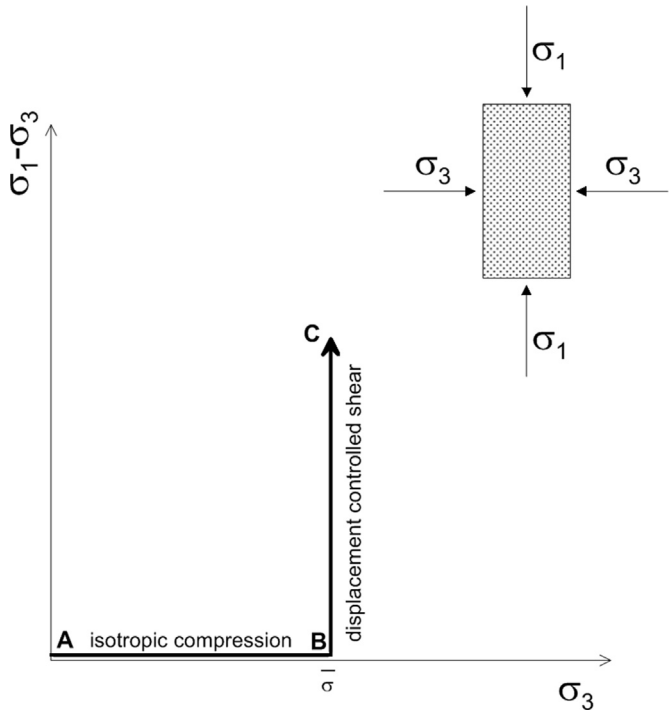

Fig. 2. Diagram of stress path for triaxial compression test.

2.2. Brazilian disc test

The tensile strength is one of the key parameters to describe the mechanical behaviour of rocks. The poor tensile resistance of rocks renders a conventional direct tension test particularly difficult. However, the tensile strength of a brittle material can be measured indirectly by means of the Brazilian disc test. The test consists of compressive loading applied to a cylindrical disc periphery. This loading condition initiates a fracture along the compressive diametral direction, where the maximum principal tensile stress is dominant. Therefore, the splitting tensile strength measured by the Brazilian test is representative of the maximum principal tensile strength of a material. The identification of the location where the maximum tensile strain takes place is another challenging issue. It can be described by a transition failure mode between a tensile failure mode that refers to as the diametral splitting fracture, and a shear failure mode, associated with the parts close to the loading platens (Li and Wong, 2013).

The Brazilian disc tests were performed on cylindrical specimens which, according to ASTM D3967-08 (2008), have a thickness to diameter ratio (t_m/d_m) of 0.2–0.75 and a specimen diameter greater than (at least) 10 times the maximum grain size. The sandstone is a medium-grained clastic sedimentary rock, with a sand size of 0.06–2 mm. The geometry data of the specimens are reported in Table 2.

According to Table 2, the specimens with an almost identical diameter were grouped into four classes based on their thickness, named G, H, I and J. As shown in Fig. 6a, the testing apparatus consists of an upper compressive platen which is displacement-controlled and a lower steel platen which is rigid. The upper platen is moved downwards to apply a compressive load. The velocity of this platen was set to 0.15 mm/min to ensure that failure occurred between 1 min and 10 min as prescribed by ASTM D3967-08 (2008).

Fig. 6b shows a specifically built steel bearing block with a curved surface. This block was positioned in between the upper platen and the specimen to decrease the contact stresses as suggested by ASTM D3967-08 (2008). Since the splitting tensile strength measured by the Brazilian test is computed based on a line load, the applied load should be limited to a narrow band. However, the narrow strip loading may create extremely high contact stresses which cause premature cracking. ASTM D3967-08 (2008) stated that if the arc of contact remains smaller than 15°, the error in deriving the principal tensile strength is less than 2%, while premature cracking is decreased dramatically. Therefore, the curvature radius of this supplementary bearing plate was designed to ensure that its arc of contact with the specimen does not exceed 15° and the width of contact is less than 6.5 mm (which refers to 40/6).

According to ASTM D3967-08 (2008), grease was used to decrease the friction between the specimen and the testing apparatus and to provide a better self-adjustment of the specimens during the loading. The applied load of the compressive platen was

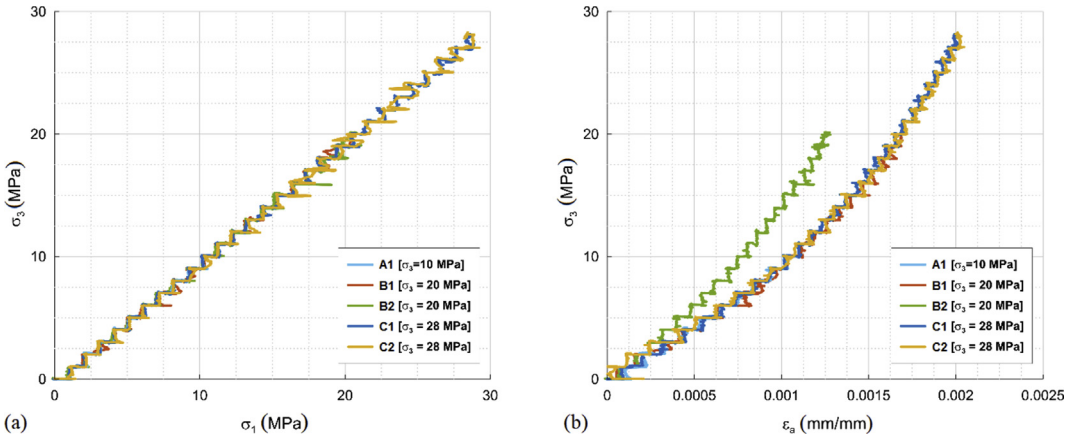

Fig. 3. Diagrams of confining stress (σ_3) vs. σ_1 and axial strain (ε_a): (a) Isotropic stage, and (b) Deviatoric stage.

measured automatically by the load cell of the apparatus. Even though the measurement of the displacement of the specimen was not described in ASTM D3967-08 (2008), it was measured by means of a displacement gauge contacting extensometer. As visible in Fig. 6a, the flexible tip of the extensometer is located at the centre of the lower face of a curved bearing block. However, since the extensometer itself is fixed to the fixture of the testing machine, the displacements of all the components in between are measured. Therefore, in the configuration shown in Fig. 6a, the experimental data provided by the extensometer contain the displacements of both the specimen and the cylindrical steel block (which is placed between the specimen and the fixture of the apparatus). This set of data therefore does not represent the actual displacement of the specimen, but since the mechanical properties of the steel blocks are known, they can be replicated in the numerical simulations as well.

The tensile splitting strength is defined as

$$\sigma_t = \frac{2F_{max}}{\pi d_m t_m} \tag{1}$$

where F_{max} is the maximum load recorded during the tests.

ASTM D3967-08 (2008) suggested reporting the repeatability limit as well. The experimental results of the Brazilian disc test in terms of the maximum force F_{max} and its corresponding displacement Δl_{max}, the average tensile splitting strength $\widehat{\sigma}_{bt}$ and repeatability limit are listed in Table 3. The ratio between the repeatability limit and the tensile splitting strength is also reported as a measure of the variability of the results.

The variability of the tensile splitting strength of all the four classes of specimens is acceptable and in agreement with the results provided by other experimental programs, i.e. ASTM D3967-08 (2008). The force-displacement diagrams of four classes are shown in Fig. 7.

Fig. 8 shows the specimens broken after the Brazilian test. The solid black lines and the dashed red lines represent the diametral loading direction and the fracture pattern, respectively. The tensile failure mode was observed for all of the specimens. The fracture pattern was independent of the thickness-to-diameter ratio with crack initiation near the interface between the specimen and the bottom steel plate and the propagation along the loading direction. The failure modes observed during the tests are in agreement with the results for sandstones under a Brazilian test reported in Basu et al. (2013), where the specimen failed by a central crack mainly parallel to the loading direction.

3. Constitutive modelling of rock materials using Karagozian and Case concrete (KCC) model

Constitutive models for geomaterials are often based on an initial yield surface coupled with a hardening rule. The subsequent yield surfaces will expand as the loading increases, resulting in a match with the failure surface (Matsuoka and Nakai, 1985). There are many studies aiming at investigating the failure function, which accordingly leads to the description of the failure surface of the geomaterial. The key feature of yielding of cohesive-frictional soil and rock materials is their mean pressure dependence. Experimental studies show that the failure surfaces of rock materials are curved and have smooth meridians. Therefore, the failure surfaces can be more conveniently described in the Haigh-Westergaard 3D stress space due to its cylindrical coordinate system. Eq. (2) can be used to transform the Cartesian coordinate system of the principal stresses into the Haigh-Westergaard system:

$$\begin{bmatrix}\sigma_1\\ \sigma_2\\ \sigma_3\end{bmatrix} = \frac{1}{\sqrt{3}}\begin{bmatrix}\xi\\ \xi\\ \xi\end{bmatrix} + \sqrt{\frac{2}{3}}\rho\begin{bmatrix}\cos\theta\\ \cos(\theta-2\pi/3)\\ \cos(\theta+2\pi/3)\end{bmatrix} \tag{2}$$

where ξ, ρ and θ are the Haigh-Westergaard coordinates defined as

$$\left.\begin{aligned} \xi &= \frac{1}{\sqrt{3}}I_1 = \sqrt{3}p \\ \rho &= \sqrt{2J_2} = \sqrt{\frac{2}{3}}\sigma_{eq} \quad (\sigma_{eq} = q) \\ \cos(3\theta) &= \left(\frac{r}{q}\right)^3 = \frac{3\sqrt{3}}{2}\frac{J_3}{J_2^{3/2}} \quad \left[r = 3\left(\frac{1}{2}J_3\right)^{1/3}\right] \end{aligned}\right\} \tag{3}$$

where I_1 is the first principal invariant of the Cauchy stress; J_2 and J_3 are the second and third principal invariants of the deviatoric part of the Cauchy stress, respectively; p is the hydrostatic pressure; and σ_{eq} is the equivalent stress.

3.1. Brief introduction to Karagozian and Case concrete (KCC) model

The failure function of the KCC material model, implemented in LS-DYNA, is characterised by a pressure-dependent yield

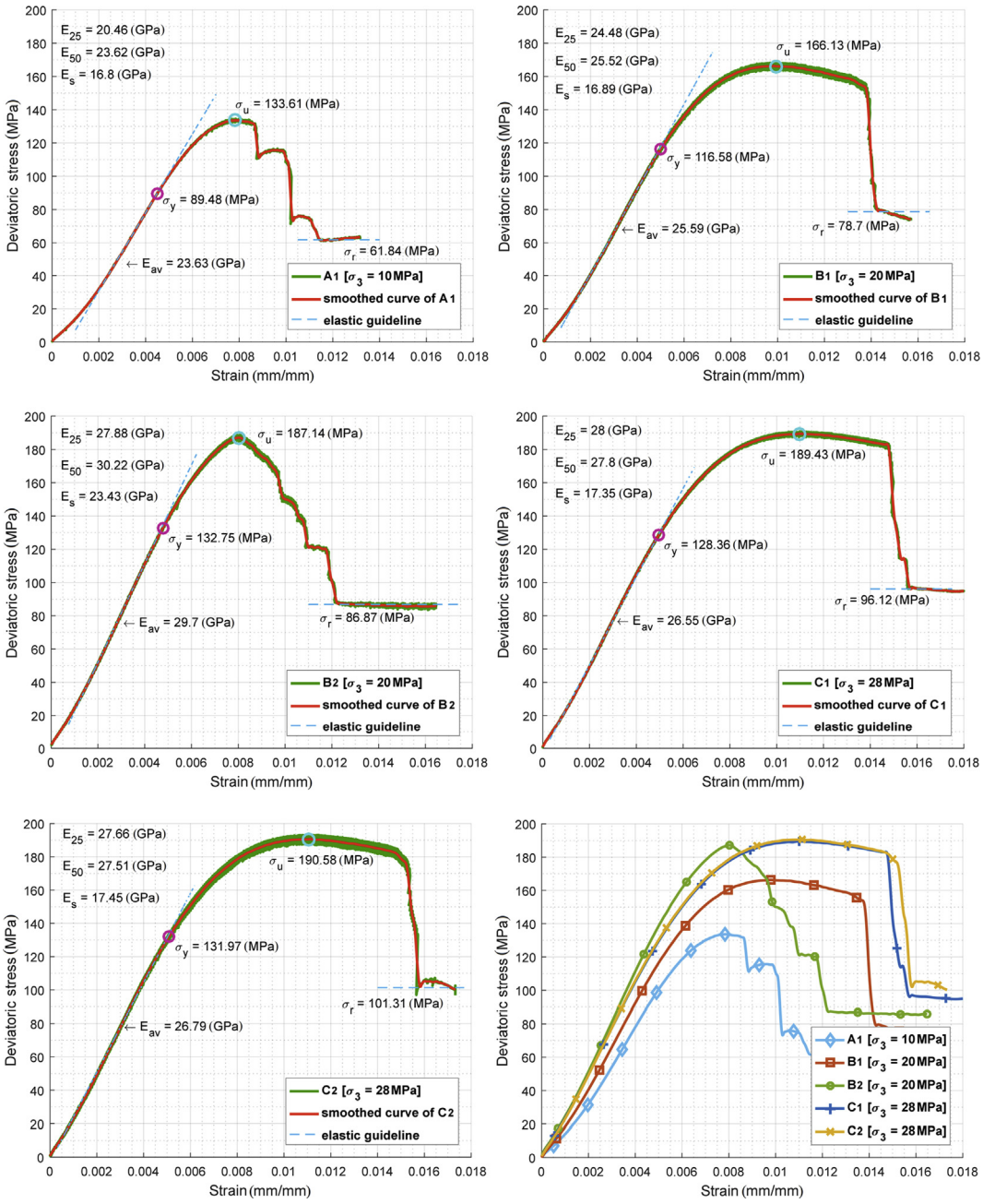

Fig. 4. Experimental results of triaxial compression tests, in terms of deviatoric stress vs. axial strain. σ_y, σ_u and σ_r denote the yield, ultimate and residual strengths, respectively; E_{25} and E_{50} represent the tangent elastic moduli at 25% and 50% of σ_u, respectively; E_s is the secant elastic modulus at 50% of σ_u; and E_{av} is the average modulus of linear portion of stress-strain curve.

surface $\Phi(\rho,\theta,\xi,\lambda)$ formulated as Eq. (4) in terms of the Haigh-Westergaard stress invariants (Malvar et al., 1997; Crawford et al., 2011):

$$\Phi(\rho,\theta,\xi,\lambda) = \sqrt{3/2}\ \rho - \varphi(\theta,\xi,\lambda) \tag{4}$$

where λ is the damage parameter in KCC model, and $\varphi(\theta,\xi,\lambda)$ is the failure surface of the KCC model.

3.2. Failure strength surfaces

The failure surface of the KCC model $\varphi(\theta,\xi,\lambda)$ is a function of the current values computed for a specific set of state variables that specify the strength of the material. The failure surface is computed by means of the linear interpolation functions that use a pair of fixed- and independent-strength surfaces which are defined by the user. These interpolation functions are different for hardening and softening. The pair for hardening and softening is denoted as the

yield-maximum and maximum-residual strength surfaces, respectively. Therefore, the $\varphi(\theta,\xi,\lambda)$ function can be described by

$$\varphi(\theta,\xi,\lambda)=\begin{cases} r_f\hat{r}[\Psi(p),\ \theta]\left[\hat{\sigma}_y(p)\right] & (\lambda\le\lambda_0)\\ r_f\hat{r}[\Psi(p),\ \theta]\{\eta(\lambda)\left[\hat{\sigma}_m(p)-\hat{\sigma}_y(p)\right]+\hat{\sigma}_y(p)\} & (\lambda_0\le\lambda\le\lambda_m)\\ r_f\hat{r}[\Psi(p),\ \theta]\{\eta(\lambda)[\hat{\sigma}_m(p)-\hat{\sigma}_r(p)]+\hat{\sigma}_r(p)\} & (\lambda_m\le\lambda)\end{cases} \tag{5}$$

where λ_0 and λ_m correspond to the points at which the hardening and softening regimes start, respectively; r_f considers the strain rate enhancement, which is beyond the scope of this article. In the KCC model, when this parameter is equal to unity, the effect of the strain rate is neglected. $\hat{\sigma}_y(p)$, $\hat{\sigma}_m(p)$ and $\hat{\sigma}_r(p)$ correspond to the yield, ultimate and residual strength surfaces in the triaxial compression state of stress, respectively, when the Lode angle θ is equal to 60° (see Fig. 9); $\eta(\lambda)$ is the interpolation damage function; and $\hat{r}\ [\Psi(p),\ \theta]$ is the non-dimensional function which is equal to the ratio between the current radius of the failure surface $r(\theta)$ (see Fig. 10b) and the distance of the failure surfaces from the hydrostatic axis at the compressive meridian r_c.

In Eq. (5), the KCC model considers the effect of the third invariant, i.e. the Lode angle θ, by means of the function $\hat{r}\ [\Psi(p),\ \theta]$. This function was originally derived from Eq. (6), which is the shape of the failure criterion in the deviatoric plane, and it was proposed by Willam and Warnke (1975):

$$r(\theta)=\frac{2r_c(r_c^2-r_t^2)\cos\theta+r_c(2r_t-r_c)\sqrt{4(r_c^2-r_t^2)\cos^2\theta+5r_t^2-4r_tr_c}}{4(r_c^2-r_t^2)\cos^2\theta+(2r_t-r_c)^2} \tag{6}$$

where $r(\theta)$ determines the distance of the failure surface at the deviatoric section by considering the effect of the Lode angle θ, and r_t expresses the distance of the failure surface from the hydrostatic axis at the tensile meridian. The deviatoric plane of a Willam-Warnke failure model is indicated in Fig. 10b.

$\hat{r}\ [\Psi(p),\ \theta]$ is computed using Eq. (7). This equation was obtained by dividing both sides of Eq. (6) by r_c. In order to present the term $\Psi(p)$, which is a strength index of the brittle material related to the confining stress (equal to $\Delta\sigma_t/\Delta\sigma_c$, and in the KCC model also equal to r_t/r_c), both the numerator and the denominator of the right-hand side of Eq. (6) are divided by $r_c{}^2$.

$$\hat{r}[\Psi(p),\ \theta]=\frac{r(\theta)}{r_c}=\frac{2(1-\Psi^2)\cos\theta+(2\Psi-1)\sqrt{4(1-\Psi^2)\cos^2\theta+5\Psi^2-4\Psi}}{4(1-\Psi^2)\cos^2\theta+(1-2\Psi)^2} \tag{7}$$

According to Eqs. (5) and (7), the parameter $\Psi(p)$ plays a significant role in determining the failure surface of the KCC model. Malvar et al. (1997) defined this parameter as a linear piecewise function on the full range of pressure:

$$\Psi(p)=\begin{cases} 1/2\ \ (-f_t\le p\le 0)\\ 1/2+3f_t/(2f_c')\ \ (p=f_c'/3)\\ \dfrac{\alpha f_c'}{a_0+\dfrac{2\alpha f_c'/3}{a_1+2a_2\alpha f_c'/3}}\ \ (p=2\alpha f_c'/3)\\ 0.753\ \ (p=3f_c')\\ 1\ \ (p\ge 8.45f_c')\end{cases} \tag{8}$$

where f_c' is the UCS, f_t is the principal tensile strength, α is an experimental parameter related to the biaxial compression test, and a_i ($i=0$, 1 and 2) are the user-defined input parameters. According to Eq. (8), $\Psi(p)$ varies from 1/2 to 1, which is in accordance with the experimental data provided by Chen (1982). It also indicates that $p=8.45f_c'$ is the transition point in which the compressive meridian is equal to tensile one, and accordingly from this point onwards, there is a circular failure surface on the deviatoric plane section. Moreover, it considers a value equal to 1/2 for the negative range of pressures. It is worth mentioning that this function is implemented in LS-DYNA (Schwer and Malvar, 2005) and no input is required by the users.

The experimental data of a triaxial compression test (the second test under confining stress of 28 MPa) were first calculated by Eq. (8) (see Fig. 11a). Based on the corresponding value of $\Psi(p)$, the function $\hat{r}[\Psi(p),\ \theta]$ was calculated and it reached to unity for the whole hardening and softening regimes, as expected ($\theta=60°$) (see Fig. 11b).

3.3. Fixed strength surfaces

The KCC model has three fixed independent failure surfaces in the compressive meridian ($\xi-\rho$ plane), which correspond to the yield, the ultimate and the residual strengths of the material, respectively. The pressure-sensitive strength surfaces of $\hat{\sigma}_y(p)$, $\hat{\sigma}_m(p)$ and $\hat{\sigma}_r(p)$ are respectively defined as (Mardalizad et al., 2018):

Table 1
Experimental results of triaxial compression test under three levels of confining pressures.

Specimen	σ_y (MPa)	σ_u (MPa)	σ_r (MPa)	E_{25} (GPa)	E_{50} (GPa)	E_s (GPa)	E_{av} (GPa)
A1	89.48	133.61	61.84	20.46	23.62	16.8	23.63
B1	116.58	266.13	78.7	24.48	25.52	16.89	25.59
B2	132.75	187.14	86.87	27.88	30.22	23.43	29.7
C1	128.36	189.43	96.12	28.01	27.83	17.35	26.55
C2	131.97	190.58	101.31	27.65	27.51	17.45	26.79

$$\widehat{\sigma}_y(p) = a_{0_y} + \frac{p}{a_{1_y} + a_{2_y}p} \text{ or } (\rho)_y = \sqrt{2/3}a_{0_y} + \frac{\sqrt{2}\xi}{3a_{1_y} + \sqrt{3}a_{2_y}\xi} \tag{9}$$

$$\widehat{\sigma}_m(p) = a_0 + \frac{p}{a_1 + a_2 p} \text{ or } (\rho)_m = \sqrt{2/3}a_0 + \frac{\sqrt{2}\xi}{3a_1 + \sqrt{3}a_2\xi} \tag{10}$$

$$\widehat{\sigma}_r(p) = \frac{p}{a_{1_f} + a_{2_f}p} \text{ or } (\rho)_r = \frac{\sqrt{2}\xi}{3a_{1_f} + \sqrt{3}a_{2_f}\xi} \tag{11}$$

The parameters a_i ($i = 0, 1$ and 2) can be calibrated based on the experimental data of the triaxial compression test by means of a curve-fitting approach. The parameters a_i of the KCC material model for the Pietra Serena sandstone, based on the triaxial compression test data, are reported in Table 4. These curves were obtained by the Curve Fitting Toolbox of MATLAB software, in which the Levenberg-Marquardt approach was considered as a fitting algorithm. The KCC failure surfaces and their corresponding experimental data are shown in Fig. 12.

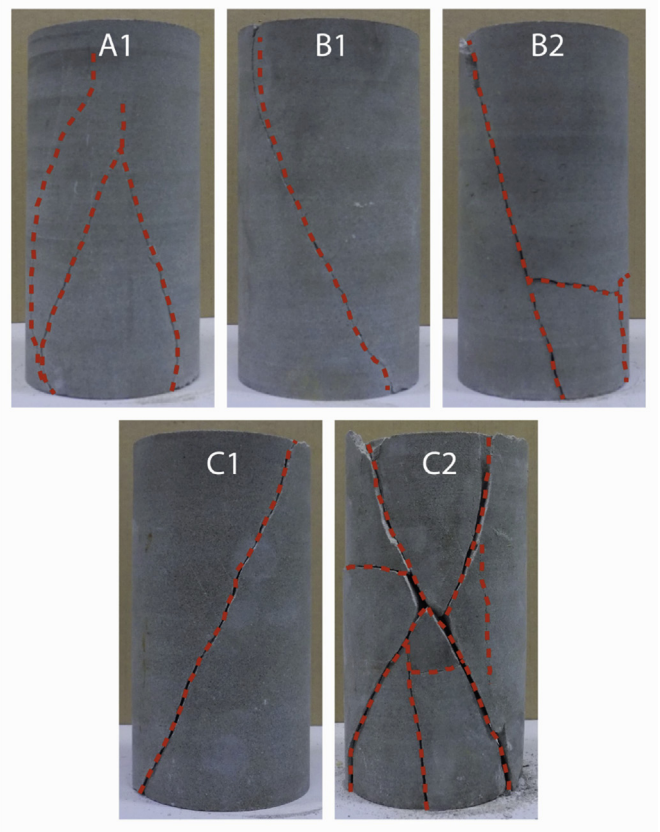

Fig. 5. Broken specimens after triaxial compression test.

3.4. Equation-of-state (EOS)

The parameter ξ in Eq. (4) is related to the pressure p which is calculated by the EOS to represent the volumetric responses. The KCC model decouples the deviatoric and volumetric responses. The deviatoric response is characterised by the migration of the current stress state between the fixed failure surfaces, while the response to pressure is defined by an EOS as a function of the volumetric strain increments. The keyword *EOS_TABULATED_COMPACTION in LS-DYNA provides a piecewise relationship between the pressure and the volumetric strain (for loading), or the bulk modulus and the volumetric strain (for unloading) according to following equation:

$$p = p^{EOS} + K\Delta\varepsilon_v^e \tag{12}$$

where p^{EOS} is the pressure from the EOS, K is the bulk modulus, and $\Delta\varepsilon_v^e$ is the incremental elastic volumetric strain. Both p^{EOS} and $\Delta\varepsilon_v^e$ can be determined by means of experimental test data, as a function of the volumetric strain. The elastic volumetric response at current step $\varepsilon_{v,n+1}^e$ in the KCC model is calculated by

$$\varepsilon_{v,n+1}^e = \ln(V_{n+1}/V_0) - \varepsilon_{v,n}^p \tag{13}$$

where V_0 and V_{n+1} are the original and current volumes, respectively; and $\varepsilon_{v,n}^p$ is the plastic volumetric strain at the previous step. The bulk modulus K in Eq. (12) is considered differently for loading and unloading scenarios. The unloading is beyond the scope of this study, but the loading bulk modulus K^L is obtained by

$$K^L = \left| \frac{p_{EOS}^{\delta} - p_{EOS}^{\delta+1}}{\varepsilon_{v,EOS}^{\delta} - \varepsilon_{v,EOS}^{\delta+1}} \right|, \ \varepsilon_{v,n+1}^{e,min} \in \left[\varepsilon_{v,EOS}^{\delta+1}, \ \varepsilon_{v,EOS}^{\delta} \right] \tag{14}$$

The subscript EOS in Eq. (14) expresses that the values related to the pressure and the volumetric strain are taken from the EOS input. The *EOS_TABULATED_COMPACTION keyword provides 10 pairs of pressure-volumetric strain data, and the superscript δ indicates the sequence on the EOS input so that $\varepsilon_{v,n+1}^{e,min} \in \left[\varepsilon_{v,EOS}^{\delta+1}, \varepsilon_{v,EOS}^{\delta} \right]$. Therefore, Eq. (12) can be represented for loading pressure by

$$p^L = p_{EOS}^{\delta} - K^L \left(\varepsilon_{v,n+1}^{e,min} - \varepsilon_{v,EOS}^{\delta} \right) \tag{15}$$

Due to the lack of a radial strain gauge device during the compression test, the experimental pressure-volumetric strain data were not measured for Pietra Serena sandstone and no other

Table 2
Geometry data corresponding to different classes of Brazilian disc test specimens.

Specimen	d_m (mm)	t_m (mm)
G1	39.7	16.1
G2	39.7	15.4
G3	39.7	16.2
H1	39.8	20.6
H2	39.8	20.7
H3	39.5	20.9
H4	39.7	20.8
H5	39.7	20.3
I1	39.6	23.9
I2	39.8	24
I3	39.7	23.9
J1	39.6	27.6
J2	39.6	27.7
J3	39.7	28.3
J4	39.6	27.7

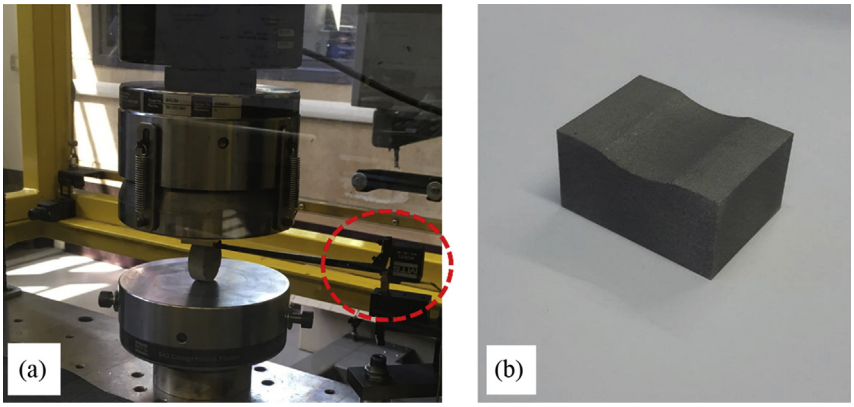

Fig. 6. (a) Brazilian disc test apparatus, based on the ASTM configuration (red circle shows the extensometer), and (b) Curved bearing block.

experimental studies of the EOS of Pietra Serena sandstone are currently available in the literature. However, in an extensive literature review (Coli et al., 2002, 2003, 2006), Berea sandstone has similar mechanical properties to the Pietra Serena sandstone. The blue curve in Fig. 13, obtained from Christensen and Wang (1985), indicates the relationship between the bulk modulus and the hydrostatic pressure of Berea sandstone.

The nonlinear least-squares curve fitting of MATLAB is exploited to consider the bulk modulus as a natural logarithmic function of the hydrostatic pressure, i.e. $K = f(p)$. By means of this function and considering $K = -V\mathrm{d}p/\mathrm{d}V$, the volumetric strain values can be written as

$$\varepsilon_{\mathrm{v,EOS}}^{\delta+1} = -\int_{p_{\mathrm{EOS}}^{\delta}}^{p_{\mathrm{EOS}}^{\delta+1}} \frac{1}{f(p)}\mathrm{d}p + \varepsilon_{\mathrm{v,EOS}}^{\delta} \tag{16}$$

To solve Eq. (16), the initial condition should be imposed as $\varepsilon_{\mathrm{v,EOS}}^{0} = p_{\mathrm{EOS}}^{0} = 0$. Therefore, the user input data of EOS as a series of pressure-volumetric strain are tabulated in Table 5. The parameter δ indicates the sequence on the EOS input.

Table 3
Experimental results of Brazilian disc test on four different specimens.

Specimen	$F_{\max}$ (kN)	$\Delta l_{\max}$ (mm)	$\widehat{\sigma}_{\mathrm{bt}}$ (MPa)
H1	7.153	0.191	5.55
H2	6.708	0.182	5.19
H3	6.445	0.203	5.22
H4	7.108	0.157	5.49
H5	7.294	0.182	5.48
Average			5.39
Repeatability			0.48
Repeatability/average ratio			0.09
J1	8.513	0.32	4.94
J2	8.772	0.279	5.09
J3	9.762	0.294	5.527
J4	7.666	0.254	4.45
Average			5.01
Repeatability			1.25
Repeatability/average ratio			0.25
G1	5.835	0.198	5.8
G2	6.155	0.177	6.39
G3	5.266	0.235	5.21
Average			5.8
Repeatability			1.67
Repeatability/average ratio			0.28
I1	7.889	0.22	5.28
I2	10.324	0.264	6.9
I3	9.145	0.283	6.15
Average			6.11
Repeatability			2.29
Repeatability/average ratio			0.37

3.5. Modified damage function

The damage evolution of the material predicted by the KCC model is depicted by the damage parameter λ, which reflects the magnitude of the plastic flow. In general, the plastic flow can be described as

$$\dot{\varepsilon}^{\mathrm{p}} = \dot{\mu}\frac{\partial g\,(\rho,\theta,\xi,\lambda)}{\partial\sigma} \tag{17}$$

where $\dot{\mu}$ is the plasticity multiplier (Wu and Crawford, 2015), and the partial-associative plastic potential of the KCC model $g(\rho,\theta,\xi,\lambda)$ can be expressed by

$$g(\rho,\theta,\xi,\lambda) = \sqrt{3/2}\rho - \omega\varphi(\theta,\xi,\lambda) \tag{18}$$

where ω is the associativity parameter that defines the proportionality between the deviatoric and volumetric components of the plastic strain. This parameter is limited between the critical values of 0 and 1, which provides associative (normal to the failure surface) and Prandtl-Reuss (plastic volume strain is precluded) forms of plasticity, respectively.

In the KCC model, the damage accumulation is imposed based on a tabular damage function, consisting of 13 pairs of η–λ parameters. The original tabular function (Malvar et al., 2000b), and the subsequent publications which presented some modifications for this function, i.e. Markovich et al. (2011) and Kong et al. (2017), focused on the concrete material. Wu et al. (2017) expressed a modified tabular function of the KCC model for asphalt concrete structures, since the corresponding strains at the peak stress of normal concretes and asphalt structures are significantly different. This publication inspired the research of a method to modify the KCC tabular damage function based on the experimental results of the triaxial compression test.

The damage accumulation of the KCC model, and accordingly the current failure surfaces are plotted schematically in Fig. 14. As shown in Fig. 14a, the state of stress is determined by a linear interpolation between the three failure surfaces. The stress-strain diagram corresponding to a typical triaxial compression test is indicated in Fig. 14c, which is determined by the associated damage accumulation function, as shown in Fig. 14b. The response of the material to the initial loading (phase I) is considered as a linearly elastic deformation before reaching Point 1. The current failure surface is therefore the same as the yield strength level $\widehat{\sigma}_{\mathrm{y}}$ at this

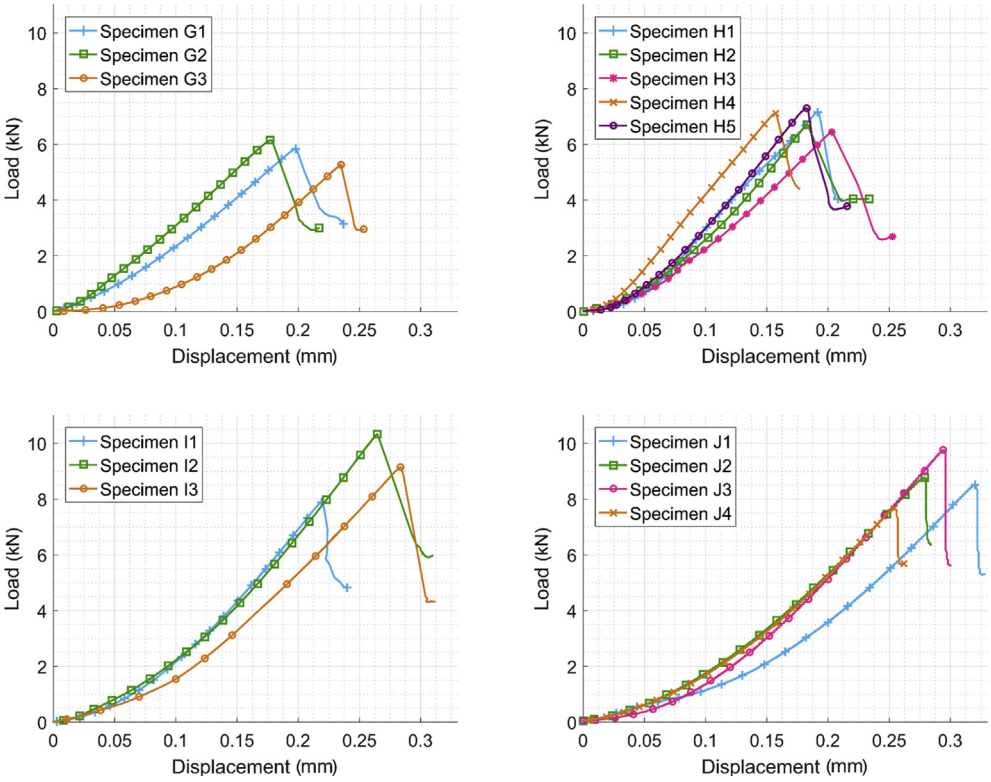

Fig. 7. Force-displacement diagrams of Brazilian disc test on four different classes of specimens.

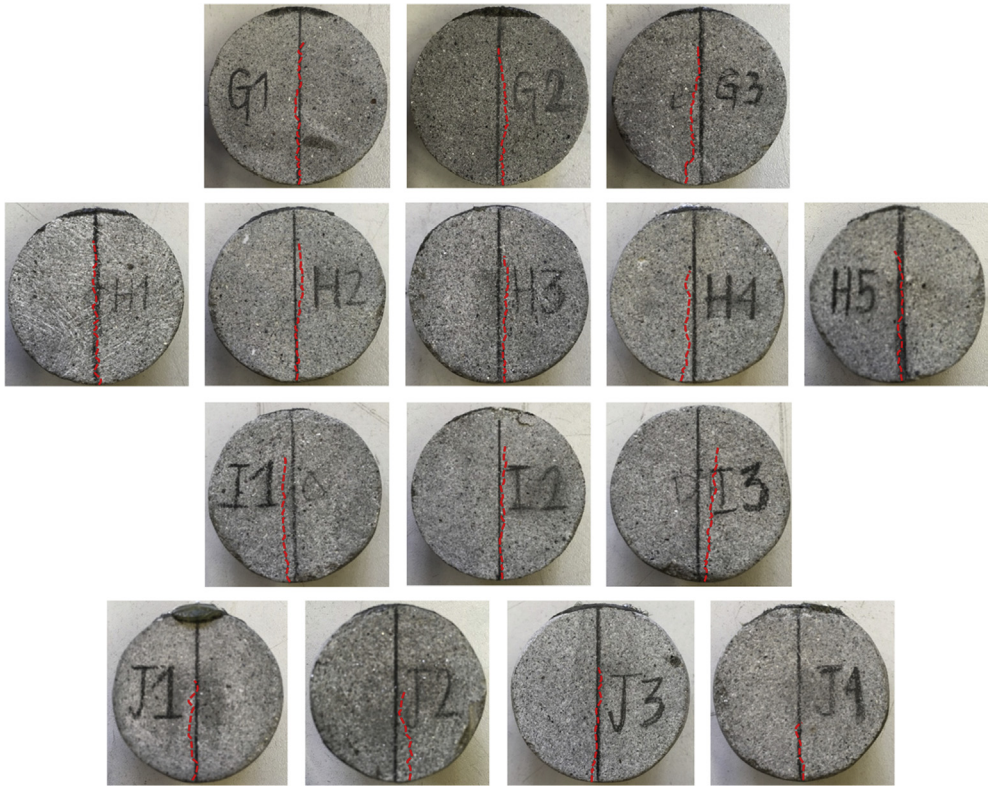

Fig. 8. Broken specimens after Brazilian disc test.

range. A hardening plasticity response occurs after yielding and before reaching the maximum strength $\widehat{\sigma}_{\mathrm{m}}$. Based on the level of the confining stress, a softening response occurs after reaching the maximum strength and before obtaining a residual strength $\widehat{\sigma}_{\mathrm{r}}$.

As shown in Fig. 14b, the damage function is imposed so that initially and prior to the occurrence of any plasticity responses, the value of η is equal to zero. It increases up to unity at a user-defined value λ_{m}, corresponding to Point 2 (the maximum strength $\widehat{\sigma}_{\mathrm{m}}$).

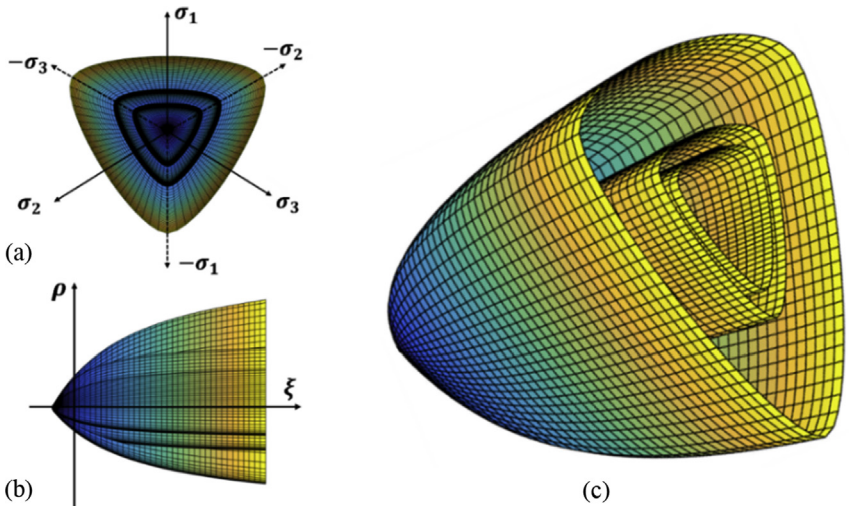

Fig. 9. KCC fixed strength surfaces: (a) Deviatoric plane, (b) Rendulic plane, and (c) 3D stress space.

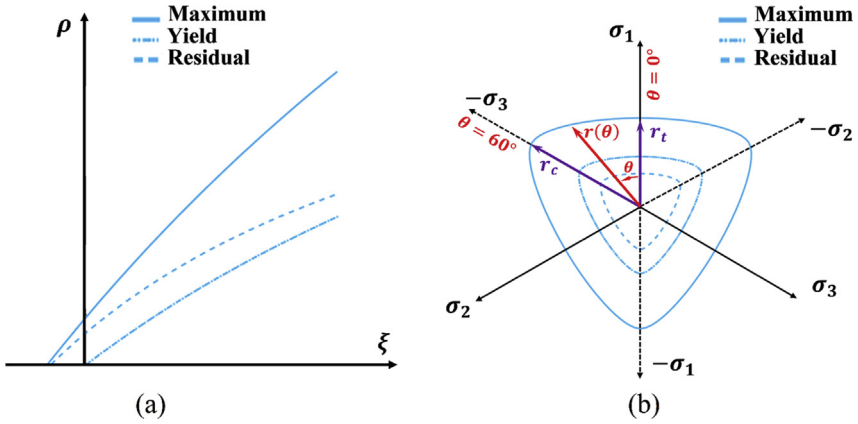

Fig. 10. (a) KCC failure surfaces in compressive meridian, and (b) Deviatoric section proposed by the Willam-Warnke model.

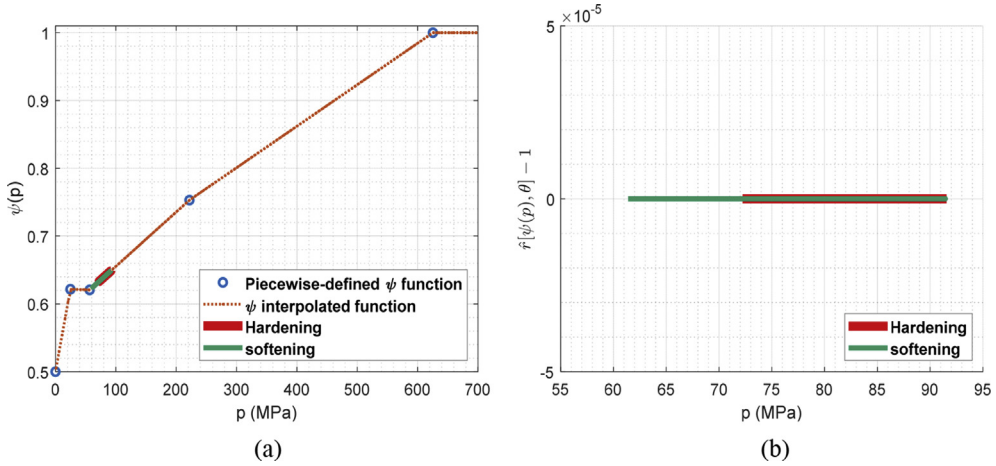

Fig. 11. Investigation of the experimental data on (a) $\Psi(p) - p$ and (b) $\hat{r}\,[\Psi(p),\ \theta] - p$ diagrams.

The KCC model considers the hardening plasticity by means of this linear-piecewise function of η–λ. After Point 2, where the softening takes place, η decreases to zero at λ_{end} corresponding to Point 3, which indicates that after this point, the current failure surface is the same as the residual strength level $\hat{\sigma}_r$. Therefore, as a first requirement to determine the tabulated damage function of the KCC model, the variations of η and λ should be in accordance with Table 6.

The strain rate tensor $\dot{\varepsilon}$ can be split into an elastic part $\dot{\varepsilon}^e$ and a plastic part $\dot{\varepsilon}^p$ in case of dealing with the small deformation/strain

Table 4
Calibrated KCC parameters a_i of Pietra Serena sandstone based on the triaxial compression tests.

Fixed strength surface	a_0 (MPa)	a_1	a_2 (MPa^{-1})
Yield surface	38.771	0.55108	6.679×10^{-4}
Maximum surface	22.645	0.50016	2.2652×10^{-3}
Residual surface	0	0.38488	3.9888×10^{-3}

regime. The evolution of the damage parameter rate $\dot{\lambda}$ is computed as a function of the plastic strain rate tensor $\dot{\bar{\varepsilon}}^{p}$ (Wu and Crawford, 2015):

$$\dot{\lambda} = h(p)\dot{\bar{\varepsilon}}^{p} \tag{19}$$

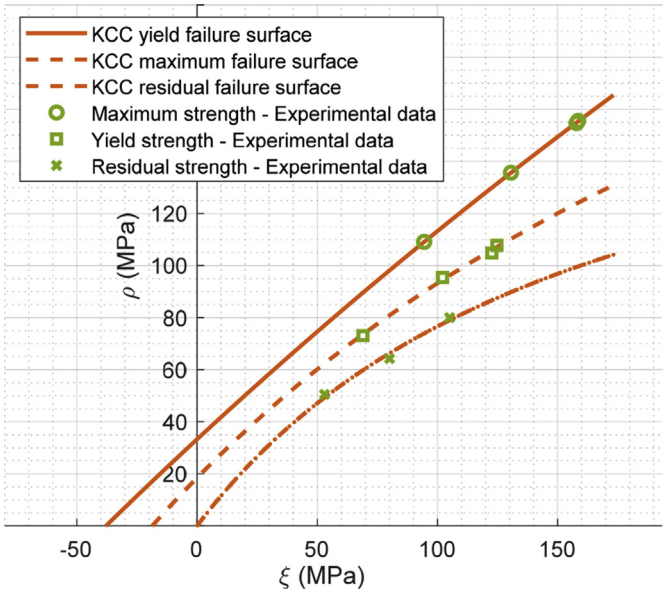

Fig. 12. Calibration of the KCC parameters a_i based on the triaxial compression tests on Pietra Serena sandstone.

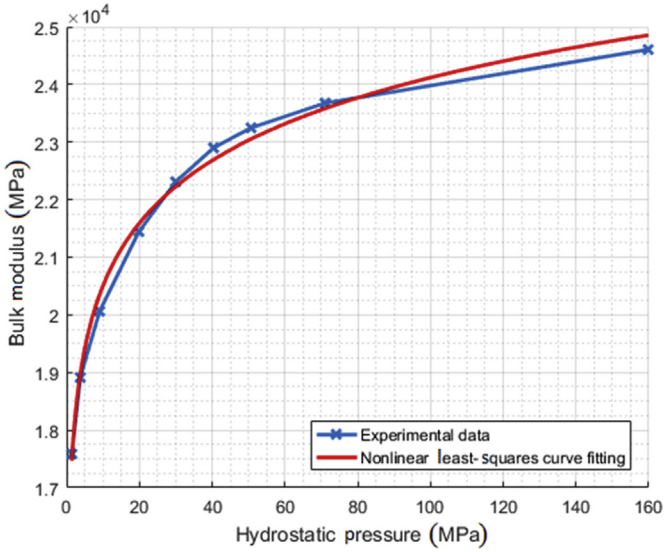

Fig. 13. Bulk modulus-hydrostatic pressure diagram of Berea sandstone (Christensen and Wang, 1985).

where $h(p)$ is the damage evolution factor given by

$$h(p) = \begin{cases} \dfrac{1}{r_f}\dfrac{1}{\left(1+\dfrac{p}{r_f f_t}\right)^{b_1}} & (p \geq 0) \\ \dfrac{1}{r_f}\dfrac{1}{\left(1+\dfrac{p}{r_f f_t}\right)^{b_2}} & (p < 0) \end{cases} \tag{20}$$

where b_1 and b_2 are the material parameters calibrated from test data, in which the first parameter governs compression and the second affects uniaxial tension. By neglecting the effect of the strain rate ($r_f = 1$), the damage parameter λ can be obtained just for the compressive (positive) range of the hydrostatic pressure as

$$\lambda = \frac{1}{\left(1+\dfrac{p}{f_t}\right)^{b_1}}\ \bar{\varepsilon}^{p}\ \ (p \geq 0) \tag{21}$$

The experimental data of the Brazilian test are used to determine f_t, and three triaxial compression test data sets (one data set that has reasonable hardening-softening behaviour under confining stress of 20 MPa, and the other two data sets under confining stress of 28 MPa) are used for determination of the hydrostatic pressure p and the equivalent plastic strain $\bar{\varepsilon}^{p}$. The parameter $\bar{\varepsilon}^{p}$ is commonly used for a von Mises isotropic hardening model (i.e. metals) which can be expressed by

$$\bar{\varepsilon}^{p} = \sqrt{\frac{2}{3}\varepsilon^{p} : \varepsilon^{p}} \tag{22}$$

where ε^{p} is the plastic strain.

Eq. (22) for an axisymmetric loading application can be simplified as

$$\bar{\varepsilon}^{p} = \sqrt{\frac{2}{3}\left[\left(\varepsilon^{p}_{axial}\right)^2 + 2\left(\varepsilon^{p}_{lateral}\right)^2\right]} \tag{23}$$

where ε^{p}_{axial} and $\varepsilon^{p}_{lateral}$ are the axial and lateral components of the plastic strain.

Due to the absence of a radial strain gauge device, the experimental data of lateral displacements were not measured during the triaxial compression tests, and only the test data of the axial strain were obtained. However, the lateral strain $\varepsilon_{lateral}$ was estimated by Eq. (24), proposed by Binici (2005) for concrete materials:

$$\left.\begin{aligned} \varepsilon_{lateral} &= -\nu\varepsilon_{axial} \quad (\varepsilon_{axial} \leq \varepsilon^{e}_{axial}) \\ \varepsilon_{lateral} &= -\nu_s\varepsilon_{axial} \quad (\varepsilon_{axial} > \varepsilon^{e}_{axial}) \end{aligned}\right\} \tag{24}$$

where ε_{axial} is the axial strain, ν is the Poisson's ratio, ε^{e}_{axial} is the axial component of elastic strain, and ν_s is the Poisson's ratio in elastic range of 0.29 (ASTM D7012-04, 2004) that was considered to be identical for Pietra Serena and Berea sandstones. The parameter ν_s is the secant Poisson's ratio that was determined by Binici (2005) for normal concrete:

$$\nu_s = \nu_l - (\nu_l - \nu)\exp\left[-\left(\frac{\varepsilon_{axial} - \varepsilon^{e}_{axial}}{\Delta\varsigma}\right)^2\right] \tag{25}$$

where

Table 5
Equation-of-state (*EOS_TABULATED_COMPACTION) for the KCC material model.

δ	ε_v	p (MPa)
1	0	0
2	−0.0001	1.4501
3	−0.0002	3.7687
4	−0.0005	9.0867
5	−0.001	19.8859
6	−0.0015	30.0015
7	−0.0019	40.3782
8	−0.0024	50.7179
9	−0.0032	71.0554
10	−0.0069	159.8497

$$\Delta\varsigma = \frac{\varepsilon_{\text{axial}}|_{\text{peak strength}} - \varepsilon^{e}_{\text{axial}}}{\sqrt{-\ln\beta}}, \quad \beta = \frac{\nu_l - \nu_p}{\nu_l - \nu},$$

$$\nu_l = \nu_p + \frac{1}{\left[\left(\frac{f_r}{f'_c}\right) + 0.85\right]^4} \tag{26}$$

where f_r is the tensile strength, and ν_p is the ratio of the lateral strain and the axial strain at the peak strain which was assumed to be 0.5. To obtain experimental values for the parameter η, Eq. (4) was considered. When the pressure-dependent surface meets the yield condition, i.e. $\Phi(\rho,\theta,\xi,\lambda) = 0$, the following equation can be derived:

$$\Delta\sigma = \sqrt{3/2}\rho = \varphi(\theta,\xi,\lambda) \tag{27}$$

By substituting $\Delta\sigma$ for $\varphi(\theta,\xi,\lambda)$ in Eq. (5), the values related to the parameter η were obtained, based on the deviatoric stress and three fixed strength surfaces according to Eq. (28). The effect of the Lode function was neglected in this equation, since the experimental data used for modification of the damage tabular function were derived from the triaxial compression test (see Fig. 11b).

Table 6
KCC damage evaluation parameters.

η	λ	Current failure surface position $\Delta\sigma$
$0 \le \eta < 1$	$0 \le \lambda < \lambda_m$	$\Delta\sigma_y \le \Delta\sigma < \Delta\sigma_m$
$\eta = 1$	$\lambda = \lambda_m$	$\Delta\sigma = \Delta\sigma_m$
$1 \ge \eta > 0$	$\lambda_m \le \lambda \le \lambda_{end}$	$\Delta\sigma_m \le \Delta\sigma < \Delta\sigma_r$

$$\left.\begin{aligned} \eta(\lambda) &= \frac{\Delta\sigma - \widehat{\sigma}_y(p)}{\widehat{\sigma}_m(p) - \widehat{\sigma}_y(p)} \quad \text{(hardening)} \\ \eta(\lambda) &= \frac{\Delta\sigma - \widehat{\sigma}_r(p)}{\widehat{\sigma}_m(p) - \widehat{\sigma}_r(p)} \quad \text{(softening)} \end{aligned}\right\} \tag{28}$$

Therefore, it is possible to transform the experimental data of the triaxial compression test from the $\Delta\sigma$–ε diagram into the η–λ diagram, by means of Eqs. (21) and (28). The parameter b_1 in Eq. (21) was used to adjust the tabular damage function, rendering the results of the numerical simulation in accordance with the experimental ones. The effect of the parameter b_1 on obtaining the KCC damage function is plotted in Fig. 15a–c for the triaxial compression test data of the 1st test under confining stress of 20 MPa, the 1st test under 28 MPa and the 2nd test under 28 MPa, respectively. These diagrams were subsequently merged in Fig. 15d for comparison.

The diagram of 'experimentally obtained values of η–λ' (by considering $b_1 = 0.75$) for a sandstone is shown in Fig. 16. Although the values of this diagram yield to a very precise response in the hardening regime, the softening gradient is found to be lower compared to the experimental results. Therefore, a new set of η–λ is presented in Fig. 16 as the 'suggested values of η–λ', that consists of the same data as the 'experimentally obtained values of η–λ' in the hardening regime, and an increased softening gradient. Further substantial proof was obtained by exploiting the present calibration in numerical simulations of the tests (virtual tests) and by comparing the results with the experimental data. These comparisons (shown in Fig. 18) imply that the numerical results stand in a reasonable agreement with the experimental data when the parameter b_1 was equal to 0.75.

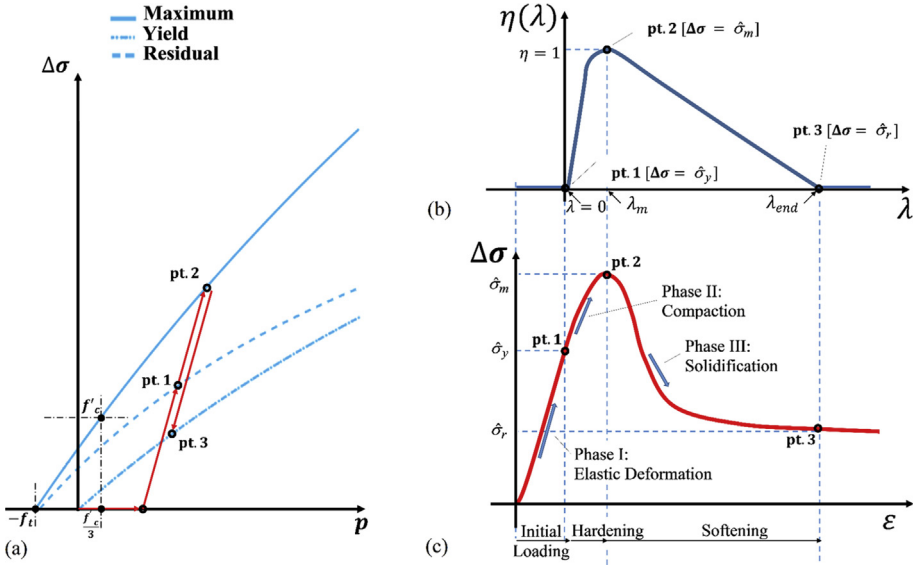

Fig. 14. Schematic representation of the KCC model: (a) Linear interpolation between the failure surfaces, (b) Damage function, and (c) A typical triaxial compression stress-strain diagram (pt. represents point).

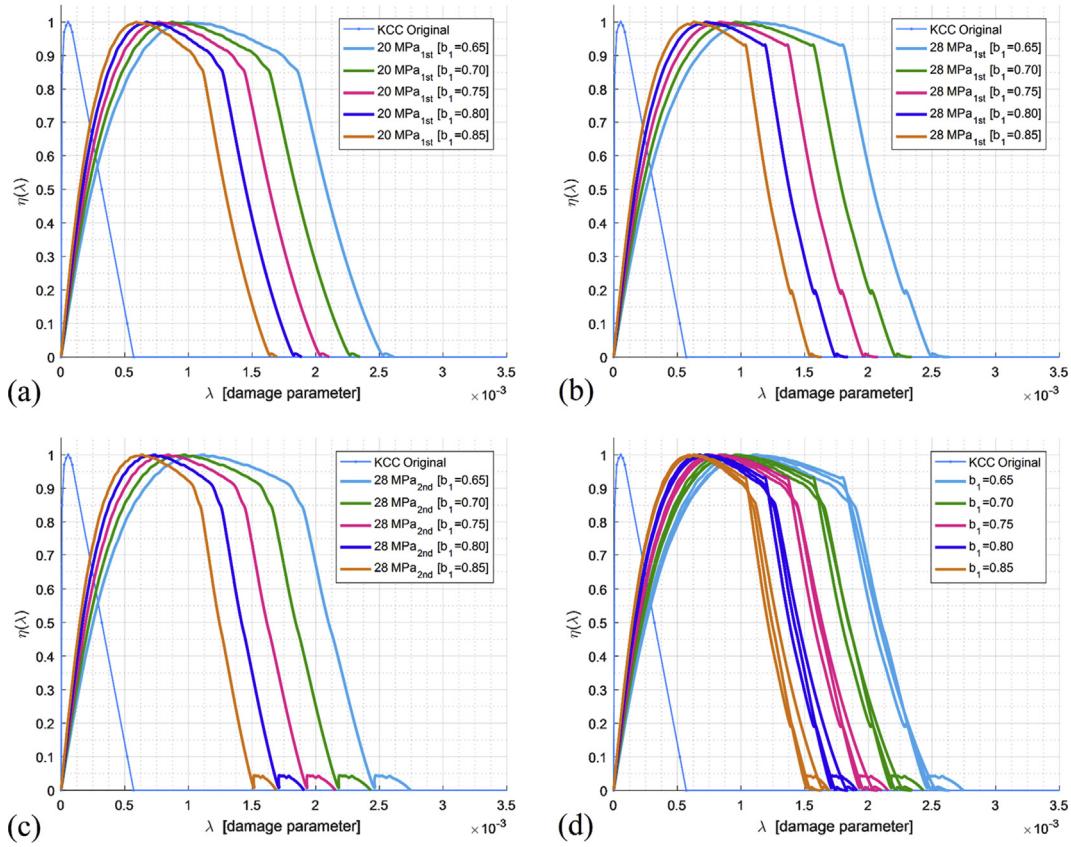

Fig. 15. Experimental representation of $\eta-\lambda$ diagrams based on the parameter b_1: (a) 1st test under confining stress of 20 MPa, (b) 1st test under confining stress of 28 MPa, (c) 2nd test under confining stress of 28 MPa, and (d) Comparison of all experimental data based on the parameter b_1 only.

It should be noted that the suggested tabular damage function was originally obtained based on Eq. (21) that governs only the compressive pressure. According to Eq. (20), the same damage evolution factor presented here, and accordingly the damage function, can be adjusted in the tensile regime by setting the parameter b_2 (and also b_3). This matter can be further investigated by performing appropriate experimental and numerical studies.

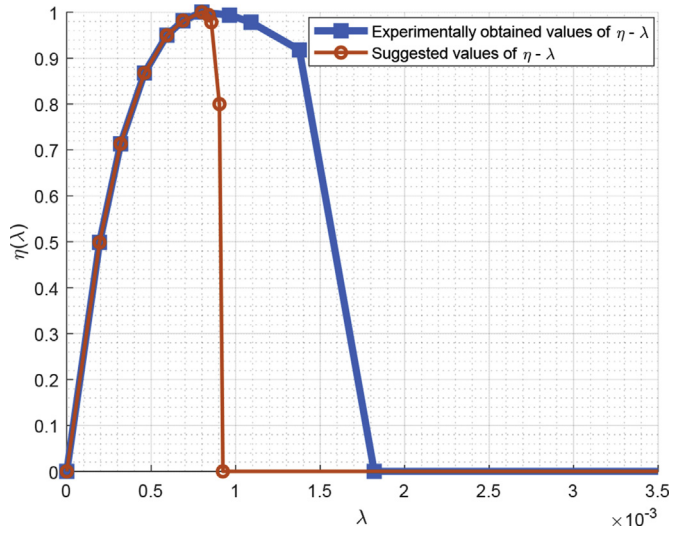

Fig. 16. Comparison of experimentally evaluated and suggested KCC tabular damage functions for rock materials.

These parameters b_i can be determined by iteration until the value of the fracture energy, G_f, converges for a specified characteristic length, which is associated with the localisation width (i.e. the width of the localisation path transverse to the crack advance).

The parameters RSIZE and UCF in the *MAT_072R3 keyword of LS-DYNA are unit conversion factors and the NOUT is called the 'output selector for effective plastic strain'. According to Hallquist (2014), when $NOUT = 2$, the quantity labelled as 'plastic strain' by the LS-PrePost is actually the quantity that describes the 'scaled damage measure, δ', which varies from 0 to 2. When the amount of

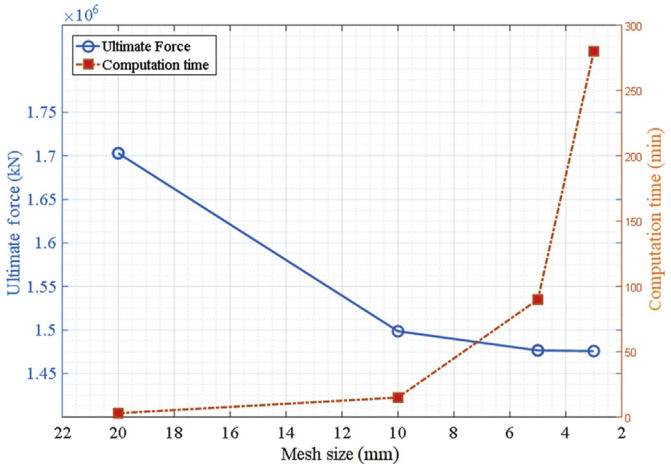

Fig. 17. Effect of mesh size on ultimate force and computation time.

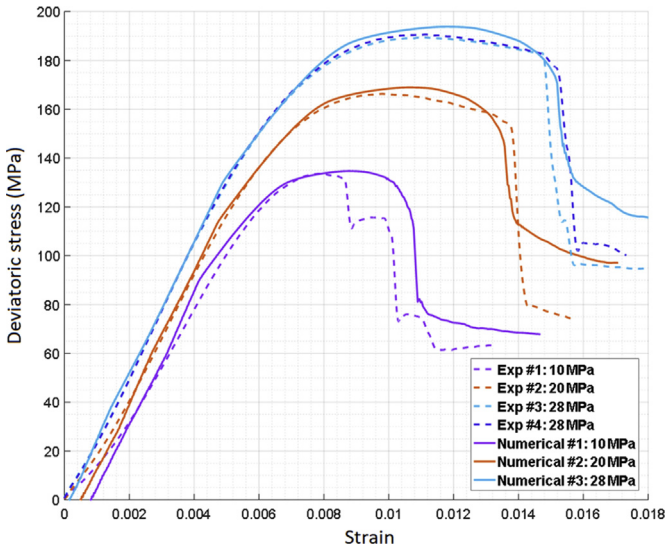

Fig. 18. Comparison between the results of the triaxial compression tests and the corresponding numerical simulations of the fully calibrated KCC material model.

δ is still lower than one, the elements of the part modelled by the KCC fail to reach the yield limit. These corresponding elements reach the yield strength at $\delta = 1$, and when $\delta = 2$, they meet their ultimate residual failure level.

4. Numerical simulation and results

In this section, three experimental arrangements were numerically replicated, i.e. the triaxial compression test, the Brazilian disc test and the flexural test. The first two numerical simulations were developed to verify the calibration procedure described in Section 3. The replication of the flexural test was subsequently performed and compared with the experimental data provided by Mardalizad et al. (2017), to show the reliability of the numerical investigations. All the experimental problems replicated in this section were solved by applying the KCC model to the sandstone. The numerical simulations concern quasi-static loading and were analysed by the FEM as provided in the explicit LS-DYNA commercial software. The numerical parts considered to replicate the sandstone were discretised by one-point Gauss quadrature integrated (*ELFORM* = 1 in LS-DYNA) solid elements. Table 7 expresses the fully calibrated KCC model, which was considered to be the default solution for the analysis of this section. The EOS for all of the models is reported in Table 5. All the geometry parts were generated, assembled and meshed by ABAQUS software and subsequently imported in LS-PrePost to specify the corresponding properties.

4.1. Triaxial compression test

The numerical model of the triaxial compression test consists of three parts: two rigid platens (representing the compressive platens) and the specimen. The rock specimen was replicated by a cylinder with the height and diameter of 200 mm and 100 mm, respectively. The displacement-controlled axial loading (compressive) was imposed by the upper platen, while the lower platen was fixed (i.e. zero degree of freedom). The confining stress was applied by *LOAD_SEGMENT_SET keyword to the exterior lateral side of the specimen and the upper platen. This confinement was applied gradually over the first 25 ms to avoid the wave propagation noise and was then kept constant. After the confining stress reached its constant final value, the upper compressive platen was pushed down at a constant velocity of 140 mm/s. This loading rate was utilised in these quasi-static analyses, since the reduction of the computation time by the time-scaling approach was more convenient. This approach requires the monitoring of the ratio of the kinetic to the internal energy during the simulations to avoid a large value (typically more than 10%).

The mesh convergence studies were performed, and the cylinder was discretised by four different sizes of meshes, i.e. 3 mm, 5 mm, 10 mm and 20 mm. Fig. 17 indicates the numerical results of the triaxial compression test under confining stress of 20 MPa obtained for these different cylinders. The results are reported in terms of the ultimate force (kN) and the computation time (min). The blue curve indicates that the mesh size of the numerical models does not influence the ultimate force when the mesh size is equal to or lower than 5 mm. In order to reduce the computation time, the cylinder with a 5-mm mesh size was considered for the numerical simulations in this section.

Table 7
Fully calibrated KCC material model for Pietra Serena sandstone.

Parameter	Value
MID	–
RO	2×10^{-9} t/mm^3
PR	0.29
FT	5.9 MPa
A0	40.771 MPa
A1	0.5511
A2	6.68×10^{-4} MPa^{-1}
B1	0.75
Omega	0.9
A1F	0.38488
Slambda	–
NOUT	2
EDROP	1
RSIZE	0.03937 in/mm
UCF	145 psi/MPa
LCRATE	–
LOCWID	1.35 mm
NPTS	13
Lambda1	0
Lambda2	1.94×10^{-4}
Lambda3	3.19×10^{-4}
Lambda4	4.60×10^{-4}
Lambda5	5.93×10^{-4}
Lambda6	7.26×10^{-4}
Lambda7	8.37×10^{-4}
Lambda8	8.69×10^{-4}
Lambda9	9.01×10^{-4}
Lambda10	9.72×10^{-4}
Lambda11	1.08×10^{-3}
Lambda12	1
Lambda13	1000
B3	0.5
A0Y	22.645 MPa
A1Y	0.50016
Eta1	0
Eta2	0.498757
Eta3	0.713508
Eta4	0.867684
Eta5	0.949989
Eta6	0.988934
Eta7	1
Eta8	0.993539
Eta9	0.978281
Eta10	0.917932
Eta11	0
Eta12	0
Eta13	0
B2	3.21
A2F	0.003989 MPa^{-1}
A2Y	0.00226 MPa^{-1}

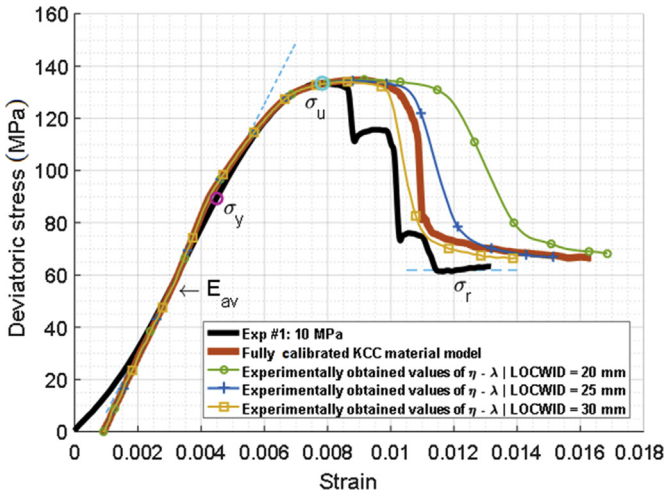

Fig. 19. Effect of the parameter LOCWID on the numerical simulation results (confining stress = 10 MPa).

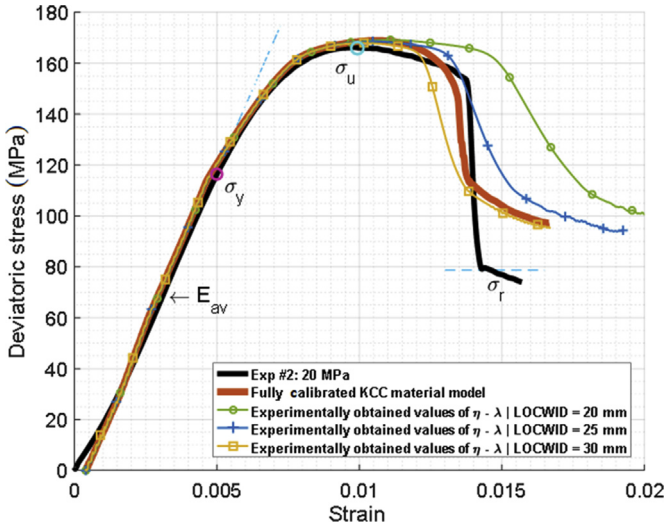

Fig. 20. Effect of the parameter LOCWID on the numerical simulation results (confining stress = 20 MPa).

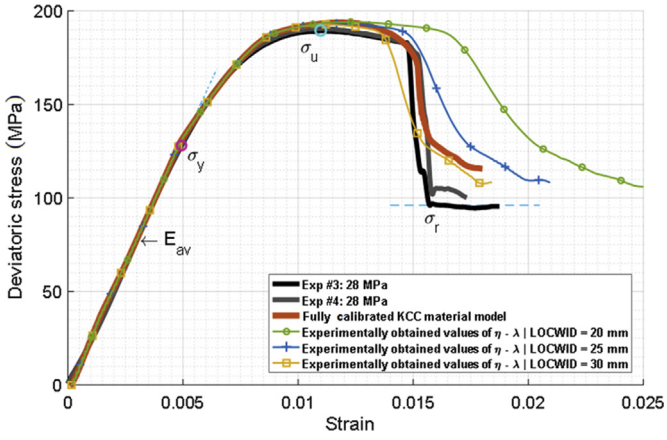

Fig. 21. Effect of the parameter LOCWID on the numerical simulation results (confining stress = 28 MPa).

Fig. 18 shows the plots of the deviatoric stress versus the axial strain computed by the fully calibrated KCC model, i.e. the η–λ damage data are the 'suggested values of η–λ' indicated in Fig. 16, for confining stresses of 10 MPa, 20 MPa and 28 MPa. The deviatoric stress expressed in this figure is the difference between the axial stress and the confining stress. The solid lines in this figure represent the results of the numerical simulation, while the dashed lines express the experimental data. The solid lines were shifted to the right so that the point corresponding to the beginning of linearly elastic regime was the same in both experimental and numerical diagrams. Thereby the effect of the settlement phase of the experimental tests (that occurs in the nonlinear regime at the beginning of the tests), which is not required to be replicated by the numerical simulations, could be neglected. Across all the confining stress levels, the results of the numerical modelling revealed reasonable agreement with the experimental results, in all of the three separate phases, i.e. linearly elastic, hardening and softening regimes. The most noteworthy features captured by this fully calibrated KCC model are related to the 'brittle- or strain-weakening'. This phenomenon is typically observed in sandstones, in which pronounced damage occurs at the softening phase and the shear plane develops yielding a sudden stress drop. This phenomenon was captured due to the damage tabular function, which was obtained based on experimental results.

Generally, there are two different methods to control the softening behaviours of materials by the KCC model: (a) the damage tabular function (η–λ diagram in which the effect of parameter b_1 is considered) and (b) the parameter LOCWID. This parameter represents the localization width (in mm), which is usually three times the maximum aggregate size for concretes. The results of the first method, as shown in Fig. 18, demonstrate that the numerical simulations precisely replicate the experimental data. The damage function implemented for these simulations is the 'suggested values of η–λ' indicated in Fig. 16. However, the sensitivity analyses based on the parameter LOCWID are expressed in Figs. 19–21 for the confining stresses of 10 MPa, 20 MPa and 28 MPa, respectively. The damage function implemented for these later simulations is the 'experimentally obtained values of η–λ' reported in Fig. 16, which was originally obtained based on experimental data. Even though the numerical results obtained by the second approach (adjusting parameter LOCWID) replicate the experimental data up to an acceptable level, the results obtained by the first approach expressed more accurate responses. This is more obvious in case of a sudden drop in the softening regime. The parameter LOCWID was able to expand the softening regime, while the gradient of the diagram was not significantly altered.

By definition, the parameter b_2 that governs the tensile regime has no influence on the triaxial compression test. Therefore, the sensitivity analyses are not reported upon this parameter. The automatic surface to surface contact treatment was defined for all the contacts, using frictional coefficients ranging from 0.1 to 0.4. The distribution of the 'scaled damage parameter' (after failure) of a triaxial compression model conducted with a coefficient of friction equal to 0.4 is shown in Fig. 22a. Additional calculations conducted with friction coefficients of 0.1, 0.2 and 0.3 gave similar results. The X-shaped damage bands of failure in Fig. 22a are observed as a function of frictional end conditions. Due to the isotropic material used in the confined compression test simulations, only the average stress-strain responses are correctly predicted while the failure mode shown in Fig. 22a is not the narrow shear bands attested in the experiments. The formation of the shear band could probably be triggered better in the simulations by introducing material or geometric imperfections.

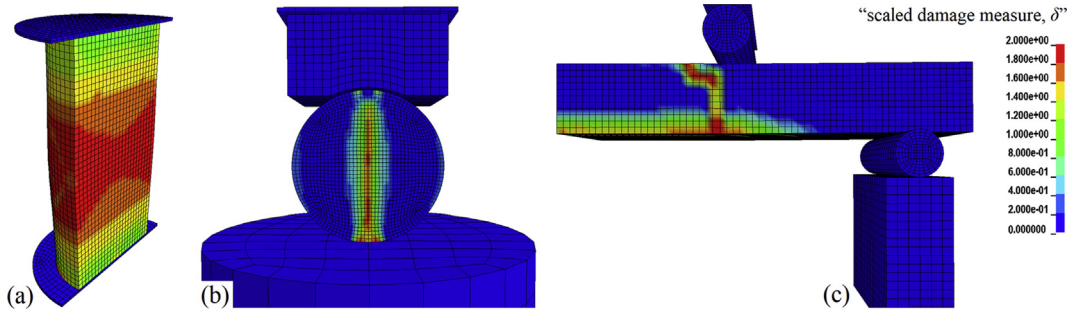

Fig. 22. Distribution of the scaled damage parameter after failure: (a) Triaxial compression test, (b) Brazilian disc test, and (c) Flexural test.

4.2. Brazilian disc test

The numerical model developed to analyse the Brazilian disc test consists of four geometry parts, which are a rigid upper compressive platen, an elastic curved bearing block, the specimen and an elastic cylindrical (steel) lower platen. The simple elastic material model (*MAT_ELASTIC in LS-DYNA) was used for the bearing block and the lower platen, by considering the elastic modulus equal to 210 GPa. Since the axial deflectometer used to measure the displacement was fixed to the bed of the apparatus, this cylindrical lower platen was modelled according to its real dimensions. The curved bearing block was also modelled in order to avoid excessive stress concentration within the numerical simulations (the same logic as that in the experimental procedure).

The part representing the sandstone specimen has the same geometry as that of the specimens of class H, with a diameter of 40 mm and a thickness of 20 mm. Similar numerical analyses were performed for the specimens with other geometries; however, they are not reported herein due to similar characteristics. This part is discretised by using one-integration point hexagonal solid elements. Mesh convergence analyses (similar to what was indicated in Section 4.1) showed that solid elements with a side dimension of lower than 1.5 mm did not influence the results. Therefore, the specimen discretised with a 1 mm mesh size was considered for the numerical simulations of this section. The displacement-controlled compressive loading was imposed by the upper platen and the bottom surface of the cylindrical lower platen was fixed (i.e. zero degree of freedom). Again, due to the quasi-static nature of this simulation, a time-scaling approach was exploited to save computation time. Therefore, the upper compressive platen was pushed down by a smooth-step function at an average velocity of 0.1 mm/ms. The automatic surface to surface contact treatment was defined for all the contacts. The distribution of the 'scaled damage parameter' (after failure) of a Brazilian disc model is shown in Fig. 22b with the failed elements clearly located along the loading diametral direction, where the principal tensile stress reaches its maximum value.

The fully calibrated KCC model and the EOS which are expressed in Tables 7 and 5, respectively, were used for the numerical simulations. However, the sensitivity analyses were performed based on the parameter b_2.

In the Brazilian disc test, the principal tensile stresses were uniformly distributed along most parts of the vertical diameter (except the areas near the two contacts). Therefore, by considering Eq. (20), the parameter b_2 was expected to have a major influence on the numerical results. The numerical results in terms of the load-displacement curves are compared in Fig. 23 with experimental data. By increasing the parameter b_2, $h(p)$ in Eq. (20) is decreased, causing a reduction of the area below the tabular damage function, rendering the material more brittle, and accordingly decreasing the failure force. Therefore, the precise value of the parameter b_2 for a material was determined by trial-and-error method. The last row of Table 8 represents the 95% confidential interval (CI) of the average value of each mechanical property. As shown in Fig. 23 and Table 8, when the parameter b_2 reaches 3.21, the best fit of the numerical results with the experimental ones can be obtained.

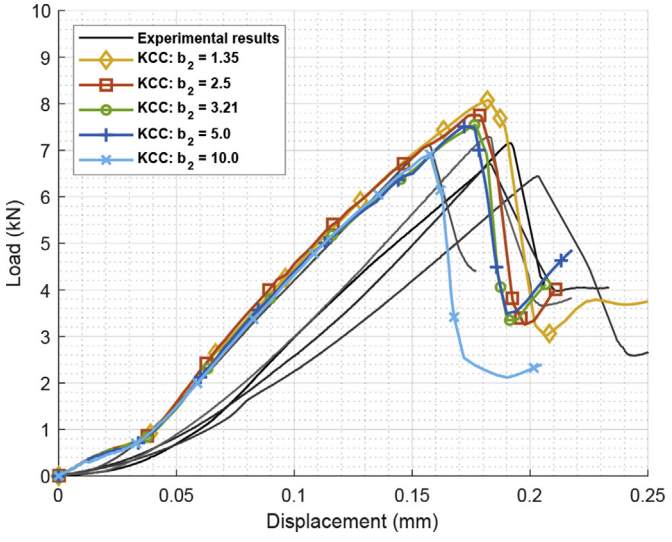

Fig. 23. Comparison of the experimental and numerical results of the Brazilian disc test, in terms of load-displacement.

4.3. Flexural test

The replication of the flexural test was performed to show the capability of the numerical investigations and the calibration procedures described. The flexural tests were performed on the same material as provided by Mardalizad et al. (2017). Accordingly, the symmetrical configuration of the four-point flexural test yields nominally zero shear forces and a constant bending moment

Table 8
Numerical results of the Brazilian disc test and comparison with the experimental data.

Parameter	F_{max} (kN)	Δl_{max} (mm)
$b_2 = 1.35$	8.075	0.182
$b_2 = 2.5$	7.752	0.178
$b_2 = 3.21$	7.531	0.177
$b_2 = 5$	7.503	0.172
$b_2 = 10$	6.91	0.157
Average of the experimental data	6.942	0.183
'95% CI' of the experimental data	6.504–7.579	0.162–0.204

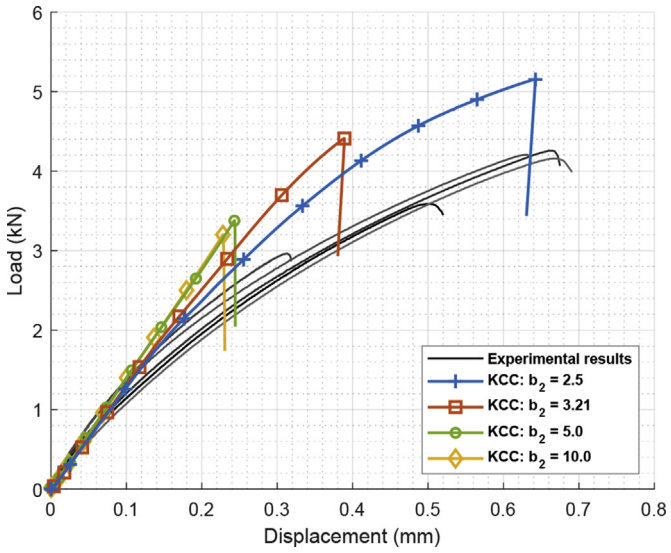

Fig. 24. Comparison of the experimental and numerical results of the flexural test, in terms of load-displacement.

between the two rollers. The principal tensile and compressive stresses are generated at the top and bottom surfaces of the specimen, respectively. Although the failure is dictated by the tensile regime (similar in almost all brittle material), the appropriate modelling of the compressive behaviour is critical to reach the final mechanical response of this application.

Due to the symmetrical nature of this experimental test, only one-quarter of the configuration was modelled. The numerical model consisted of five components, which were the upper compressive platen, two rollers, the specimen and the support steel block. The simple elastic material model (*MAT_ELASTIC in LS-DYNA) was used for both the aluminium rollers and the support steel block, by considering their elastic modulus equal to 70 GPa and 210 GPa, respectively. Since the axial deflectometer used to measure the displacement was fixed to the bed of the apparatus, the support block was modelled on its real dimensions.

The geometry of the part representing the sandstone specimen was the same as the experimental one, with a length of 318 mm, a width of 102 mm and a height of 32 mm. This part was discretised by using one-integration point hexagonal solid elements with a side dimension of 3 mm. The displacement-controlled compressive loading was imposed by the upper rigid platen and the bottom surface of the steel support block was fixed (i.e. zero degree of freedom). Similar to the two previous simulations, the time-scaling approach was used to save computation cost. Therefore, the upper compressive platen was pushed down at a constant velocity of 9 mm/s. The automatic surface to surface contact treatment was defined for all the contacts. The fully calibrated KCC model and the EOS which are expressed in Tables 7 and 5, respectively, were used for the numerical simulations. The sensitivity analyses were also performed based on the parameter b_2.

Table 9
Numerical results of the flexural test in comparison with the experimental data.

Parameter	F_{max} (kN)	Δl_{max} (mm)
$b_2 = 2.5$	5.157	0.642
$b_2 = 3.21$ (Fully calibrated KCC)	4.411	0.389
$b_2 = 5$	3.376	0.243
$b_2 = 10$	3.198	0.228
Average of the experimental data	3.835	0.554
'95% CI' of the experimental data	3.143–4.527	0.367–0.742

The numerical results are expressed in terms of force-displacement diagrams in Fig. 24 and were subsequently compared with the experimental ones. Identical to the Brazilian disc test, due to the presence of the principal tensile stresses at the lower surface of the specimen, the parameter b_2 was shown to have great influence on the results. The value of the parameter b_2 determined by the Brazilian disc test (i.e. equal to 3.21) yielded the best response also in the flexural test. The numerical results, both in terms of the ultimate force and the maximum displacement, were found to lie within the 95% CI of the experimental values (see Table 9). As described in Mardalizad et al. (2017), ASTM D3967-08 (2008) fails to provide any recommendations for capturing the displacement data and therefore an axial deflectometer was used to measure these data. The deflectometer was attached to the fixture of the apparatus and hence, as stated above, the displacement corresponding to all the components between the rock and the fixture was measured in the experimental results, causing the difference between the ultimate axial displacement levels in the numerical and experimental results. The distribution of the 'scaled damage parameter' (after failure) of a flexural model is shown in Fig. 22c. The comparison of the failed elements in this model and the experimental results, provided in Mardalizad et al. (2017), shows that the numerical simulation precisely replicates the experimental crack pattern.

5. Conclusions

The mechanical response of a rock material was investigated by means of experimental tests and finite element modelling that exploits an advanced KCC material model. The procedure proposed for calibrating the KCC model was investigated specifically for Pietra Serena sandstone but can also be used for other rock materials. This calibration procedure was mainly based on an experimental approach aiming to overcome the main drawback of the KCC model; the long set of data was required as input parameters. The automatic input generation mode (implemented in the 3rd release of the KCC in LS-DYNA) is not aimed to realistically predict the mechanical response of other types of quasi-brittle materials other than concrete. The experimental test required for this calibration method consists of two programs, i.e. the triaxial compression and the Brazilian disc tests, to characterise the material deviatoric responses in compressive and tensile regimes, respectively.

The input parameters were investigated and classified into five distinct categories: tensile strength, failure (fixed) strength surfaces, tabular damage function, EOS and damage parameters. The quasi-static Brazilian disc test was used to measure the ultimate principal tensile strength. The triaxial compression test, with three levels of confining stresses, was carried out to determine the other groups. The yield, the ultimate and the residual strengths measured via the experimental tests were used to determine the parameters a_i, which are the KCC input parameters to describe the fixed strength surfaces. Since the KCC model decouples the deviatoric and volumetric responses, the experimental data of the isotropic stage (of triaxial compression test) can be potentially used to define the EOS for a given material. However, due to the absence of an appropriate laboratory device to measure the radial displacement, the EOS dedicated to the material under investigation in this study was determined analytically, based on the experimental data of the axial displacement. A modification to the tabular damage function was suggested based on the experimental data of the triaxial compression test in the deviatoric stage. Finally, through exploiting the availability of the numerical models, a sensitivity analysis was performed to determine the parameters b_i, which are the damage parameters of the KCC material model.

Therefore, a material model specifically calibrated with the required full set of input data was developed for Pietra Serena sandstone. The fully calibrated material model was implemented in the finite element codes of the explicit LS-DYNA to replicate the experimental tests (verification). The numerical results for both the triaxial compression and the Brazilian tests were consistent with the experimental test results. The fully calibrated material model was then further investigated by replicating a flexural (four-point bending) test, which includes both the compressive and tensile stresses. The critical comparison between the numerical and the experimental test results demonstrated the capability and precision of the procedure proposed.

Conflicts of interest

We wish to confirm that there are no known conflicts of interest associated with this publication and there has been no significant financial support for this work that could have influenced its outcome.

References

ASTM D3967-08. Standard test method for splitting tensile strength of intact rock core specimens. West Conshohocken, PA, USA: ASTM International; 2008.

ASTM D7012-04. Standard test method for compressive strength and elastic moduli of intact rock core specimens under varying states of stress and temperatures. West Conshohocken, PA, USA: ASTM International; 2004.

Bai M, Meng F, Elsworth D, Abousleiman Y, Roegiers JC. Numerical modelling of coupled flow and deformation in fractured rock specimens. International Journal for Numerical and Analytical Methods in Geomechanics 1999;23(2):141–60.

Basu A, Mishra D, Roychowdhury K. Rock failure modes under uniaxial compression, Brazilian, and point load tests. Bulletin of Engineering Geology and the Environment 2013;72(3–4):457–75.

Binici B. An analytical model for stress–strain behavior of confined concrete. Engineering Structures 2005;27(7):1040–51.

Brady BH, Brown ET. Rock mechanics: for underground mining. Springer Science & Business Media; 2013.

Brannon RM, Leelavanichkul S. Survey of four damage models for concrete. Sandia Report No. SAND 2009-5544. Albuquerque, USA: Sandia Laboratories; 2009.

Chen W. Plasticity in reinforced concrete. New York, USA: McGraw-Hill; 1982.

Chen SH, Egger P. Three dimensional elasto-viscoplastic finite element analysis of reinforced rock masses and its application. International Journal for Numerical and Analytical Methods in Geomechanics 1999;23(1):61–78.

Christensen N, Wang H. The influence of pore pressure and confining pressure on dynamic elastic properties of Berea sandstone. Geophysics 1985;50(2):207–13.

Cividini A, Taliercio A, Landriani GS, Bellotti R, Ferrara G, Rossi P. An apparatus for cyclic tests on cylindrical concrete specimens. Materials and Structures 1992;25:490.

Clausi M, Magnani LL, Occhipinti R, Riccardi MP, Zema M, Tarantino SC. Interaction of metakaolin-based geopolymers with natural and artificial stones and implications on their use in cultural heritage. International Journal of Conservation Science 2016;7(2):871–84.

Coli M, Livi E, Tanini C. Pietra Serena in fiesole. Part I: historical, cultural, and cognitive aspects. Journal of Mining Science 2002;38(3):251–5.

Coli M, Livi E, Tanini C. Pietra Serena in fiesole. Part II: geological setting and quarrying. Journal of Mining Science 2003;39(1):56–63.

Coli M, Livi E, Tanini C. Pietra Serena mining in fiesole. Part III: structural-mechanical characterization and mining. Journal of Mining Science 2006;42(1):74–84.

Cornelissen H, Hordijk D, Reinhardt H. Experimental determination of crack softening characteristics of normalweight and lightweight concrete. HERON 1986;31(2):45–56.

Crawford J, Magallanes J, Lan S, Wu Y. User's manual and documentation for release III of the K&C concrete material model in LS-DYNA. K&C Technical Report TR-11-36. 2011.

Desmorat R, Gatuingt F, Ragueneau F. Nonlocal anisotropic damage model and related computational aspects for quasi-brittle materials. Engineering Fracture Mechanics 2007;74(10):1539–60.

Fossum A, Brannon R. Unified compaction/dilation, strain-rate sensitive, constitutive model for rock mechanics structural analysis applications. In: Gulf rocks 2004, proceedings of the 6th North America rock mechanics Symposium (NARMS). American Rock Mechanics Association; 2004.

Gary G, Bailly P. Behaviour of quasi-brittle material at high strain rate. Experiment and modelling. European Journal of Mechanics A Solids 1998;17(3):403–20.

Hallquist JO. LS-DYNA® keyword user's manual: volumes I, II, and III. Livermore, California, USA: Livermore Software Technology Corporation (LSTC); 2014.

Hu Y, Randolph M. A practical numerical approach for large deformation problems in soil. International Journal for Numerical and Analytical Methods in Geomechanics 1998;22(5):327–50.

Huang X, Karihaloo B. Micromechanical modelling of the tensile behaviour of quasi-brittle materials. In: Advances in engineering plasticity and its applications. Elsevier; 1993.

Jaeger JC, Cook NGW, Zimmerman RW. Fundamentals of rock mechanics. Wiley-Blackwell; 2007.

Jaime MC. Numerical modeling of rock cutting and its associated fragmentation process using the finite element method (PhD Thesis). University of Pittsburgh; 2011.

Jing L, Hudson J. Numerical methods in rock mechanics. International Journal of Rock Mechanics and Mining Sciences 2002;39(4):409–27.

Kochavi E, Kivity Y, Anteby I, Sadot O, Ben-Dor G. Numerical modeling of composite concrete-durisol walls. In: Proceedings of the 20th international Symposium on military aspects of blast and Shock; 2008.

Kochavi E, Kivity Y, Anteby I, Sadot O, Ben-Dor G. Numerical model of composite concrete walls. In: Proceedings of the 9th biennial ASME conference on engineering systems design and analysis. American Society of Mechanical Engineers (ASME); 2008b.

Kong X, Fang Q, Li Q, Wu H, Crawford JE. Modified K&C model for cratering and scabbing of concrete slabs under projectile impact. International Journal of Impact Engineering 2017;108:217–28.

Kuhl E, Ramm E, de Borst R. An anisotropic gradient damage model for quasi-brittle materials. Computer Methods in Applied Mechanics and Engineering 2000;183(1–2):87–103.

Labuz J, Shah S, Dowding C. Experimental analysis of crack propagation in granite. Experimental analysis of crack propagation in granite. International Journal of Rock Mechanics and Mining Sciences and Geomechanics Abstracts 1985;22(2):85–98.

Lacy WC, Lacy JC. History of mining. In: SME mining engineering handbook; 1992.

Li D, Wong LNY. The Brazilian disc test for rock mechanics applications: review and new insights. Rock Mechanics and Rock Engineering 2013;46(2):269–87.

Li L, Lee PKK, Tsui Y, Tham LG, Tang CA. Failure process of granite. International Journal of Geomechanics 2003;3(1):84–98.

Malvar LJ, Crawford JE. Dynamic increase factors for concrete. DTIC Document; 1998.

Malvar LJ, Crawford JE, Wesevich JW, Simons D. A plasticity concrete material model for DYNA3D. International Journal of Impact Engineering 1997;19(9–10):847–73.

Malvar L, Crawford J, Wesevich J, Simons D. A new concrete material model for DYNA3D. Technical Report No. TR94-14.3. Karagozian & Case; 1994.

Malvar LJ, Crawford JE, Wesevich JW. A concrete material model for DYNA3D. In: Proceedings of the 10th ASCE engineering mechanics conference; 1995.

Malvar L, Crawford J, Morill K. K&C concrete material model release III: automated generation of material model input. Technical Report TR-99-24-B1. Karagozian & Case; 2000a.

Malvar LJ, Crawford JE, Morrill KB. K&C concrete material model release III-automated generation of material model input. Technical Report TR-99-24-B1. Karagozian & Case; 2000b.

Mardalizad A, Scazzosi R, Manes A, Giglio M. Four-point bending test on a middle strength rock: numerical and experimental investigations. Frattura ed Integrità Strutturale 2017;11(41):504–23.

Mardalizad A, Scazzosi R, Manes A, Giglio M. Testing and numerical simulation of a medium strength rock material under unconfined compression loading. Journal of Rock Mechanics and Geotechnical Engineering 2018;10(2):197–211.

Markovich N, Kochavi E, Ben-Dor G. An improved calibration of the concrete damage model. Finite Elements in Analysis and Design 2011;47(11):1280–90.

Martin CD. The strength of massive Lac du Bonnet granite around underground openings (PhD Thesis). Winnipeg, Manitoba, Canada: University of Manitoba; 1993.

Matsuoka H, Nakai T. Relationship among Tresca, Mises, Mohr-Coulomb and Matsuoka-Nakai failure criteria. Soils and Foundations 1985;25:123–8.

Pepper JF. Geology of the bedford shale and Berea sandstone in the appalachian basin: a study of the stratigraphy, sedimentation and paleogeography of rocks of bedford and Berea age in Ohio and adjacent states. US Government Printing Office; 1954.

Rots JG, De Borst R. Analysis of mixed-mode fracture in concrete. Journal of Engineering Mechanics 1987;113(11):1739–58.

Saksala T. Damage-viscoplastic consistency model with a parabolic cap for rocks with brittle and ductile behavior under low-velocity impact loading. International Journal for Numerical and Analytical Methods in Geomechanics 2010;34(13):1362–86.

Santarelli FJ, Brown ET. Failure of three sedimentary rocks in triaxial and hollow cylinder compression tests. International Journal of Rock Mechanics and Mining Sciences and Geomechanics Abstracts 1989;26(5):401–13.

Schwer LE, Malvar LJ. Simplified concrete modeling with *mat-concrete-damage-rel3. In: JRI LS-DYNA user week; 2005.

Willam K, Warnke E. Constitutive model for the triaxial behavior of concrete. In: Proceedings of international association for bridge and structural engineering; 1975. p. 1–30.
Winnicki A, Pearce C, Bićanić N. Viscoplastic Hoffman consistency model for concrete. Computers and Structures 2001;79(1):7–19.
Wu Y, Crawford JE. Numerical modeling of concrete using a partially associative plasticity model. Journal of Engineering Mechanics 2015;141(12). https://doi.org/10.1061/(ASCE)EM.1943-7889.0000952.
Wu J, Li L, Du X, Liu X. Numerical study on the asphalt concrete structure for blast and impact load using the Karagozian and case concrete model. Applied Sciences 2017;7(2). https://doi.org/10.3390/app7020202.
Zhao H, Zhang C, Cao WG, Zhao MH. Statistical meso-damage model for quasi-brittle rocks to account for damage tolerance principle. Environmental Earth Sciences 2016;75:1–12.

Aria Mardalizad obtained his PhD from Department of Mechanical Engineering of the Politecnico di Milano, Italy. He obtained his BSc degree in Mechanical Engineering – Solid Mechanics from the Guilan University, Rasht, Iran in 2011. He received his MSc degree in Mechanical Engineering from Politecnico di Torino, Italy, in 2015. His recent research interest has been on the mechanical properties of quasi-brittle materials, by numerical and experimental investigations. His PhD studies include different techniques of numerical simulations, as well as constitutive modelling of geotechnical materials.

Marco Caruso received a PhD in geotechnical engineering and is the head of Geotechnical division of Material Testing Laboratory at Politecnico di Milano. His activity was mainly addressed to problems related to environment and land protection, with special attention to the experimental characterisation of soils (especially unsaturated) and rocks by laboratory tests and site investigations. His interests are also in design, development and set-up of new advanced testing devices and small to medium-scale models for understanding of complex geotechnical and environmental systems. Recently, he also focuses on hydro-mechanical behaviour of compacted earth as materials for sustainable building and its related experimental approaches. He collaborated with several companies and public institutions in the framework of research and industry-oriented projects.

Andrea Manes is Associate Professor at School of Industrial Engineering, Department of Mechanical Engineering, Politecnico di Milano. His main research topics are in the field of advanced engineering approaches for structural integrity, assessment and design of mechanical, aerospace and O&G components and systems: (i) assessment and optimisation of components and systems under static, spectrum/fatigue and extreme loads; (ii) application of novel approaches in structural integrity design (flaw tolerant, vulnerability, condition based, etc.); (iii) investigation in mechanical behaviour of materials (metals, composite, ceramic, rock); (iv) expertise in nonlinear numerical modelling techniques (including meshless methods); and (v) monitoring, diagnosis and prognosis of critical structures under fatigue loads and impact loads. He had participated to several European, National and industrial projects. He had published more than 130 papers mainly in referred international journals and congresses. He was Visiting Professor at Tongji University (Shanghai, China) in 2013 and Visiting Scientist at Norwegian University of Science and Technology (NTNU) - SIMLab, Trondheim (Norway) in 2009.

Marco Giglio is Full Professor at Department of Mechanical Engineering, School of Industrial Engineering (Bovisa), Politecnico di Milano. His research interest covers structural integrity evaluation on aircraft and mechanical structures with the use of structural health monitoring methodologies, assessment of ballistic impact damage on components and structures in mechanical and aeronautical fields, calibration of constitutive laws for metallic materials, expected fatigue life and crack propagation behaviour on aircraft structures and components, and fatigue design with defects. He is the author and co-author of more than 70 publications in peer-reviewed international journals and book chapters and more than 100 publications in international and national conference proceedings. Dr. Giglio is the coordinator or leader for several European and national projects. He won the Best Paper Award of Prognostics and Health Management Society for the paper '*Optimal tuning of particle filtering random noise for monotonic degradation processes*' (M. Corbetta, C. Sbarufatti, M. Giglio). He is also the reviewer of regional and national projects for the Ministry of Education, University and Research (MIUR) in Aerospace and Mechanical Engineering, and expert inserted in the Register of the MIUR - DD n. 79/2010/Ric, defined after international public selection in 2011.